Chaos in the Canopy

Unraveling Uses of Fiber Optics in the Forest

Anika L. Vroom

Chaos in the Canopy

Unraveling Uses of Fiber Optics in the Forest

by

Anika L. Vroom

to obtain the degree of Master of Science
at the Delft University of Technology,
to be defended publicly on Tuesday July 4, 2023, at 14:00.

Student number:	44894916	
Project duration:	February 29, 2022 – July 4, 2023	
Thesis committee:	A. M. J. Coenders-Gerrits,	TU Delft (chair)
	L. D. van der Valk,	TU Delft
	B. J. H. van de Wiel,	TU Delft
	M. K. van der Molen,	Wageningen University

This thesis is confidential and cannot be made public until July 4, 2023.

TU Delft

Acknowledgements

From March through December of 2022, this project progressed in much the same manner as it's subject of study, which is to say, with a fair amount of turbulence. During these months, I planned and carried out a different, but related, research project, one concerning a 2D Distributed Temperature Sensor (DTS) set-up. As I reviewed the data in September and October, it slowly dawned that something was amiss with the data. By the time November hit, I had pinpointed a material error concerning the thickness of the core inside of the optic fiber (something impossible to discern with the naked eye), and by December I had begrudgingly accepted that I would need a new research question, data set, and analysis process. It is from this new starting point that we commence the real story, the one told in the rest of these pages.

Many hands made the process of chasing after the upcoming colorful assortment of canopy-related correlations and patterns possible. My predecessors and partners in crime: Luuk, Bas, Gijs, Dai, and Judith, thank you for the advice, joining my fieldwork excursions, and transforming the DTS from a confusing, unapproachable, and extremely expensive mystery box into a tamed beastie. Thank you to my committee for seeing me through this project: Miriam, for the countless meetings, brainstorming sessions, and detailed advice; Luuk, not only for the trips out to Loobos, but also the detailed edits and a fair dose of encouragement (the effect of which is not to be underestimated in the face of "shelving" months of work); Michiel, for providing project design advice and key data; and Bas, for new insights and a critical eye into where some of my problem areas might reside. For all the edits, late-night discussions, and proofreading, thank you to Vita, Elizabeth, and Herman. Lastly, a massive thank-you to those who had no stakes (or particular reason to be interested) in this project, yet suffered through climbing up small staircases in the wind, untangling hundreds of meters of fishline-like fiber, and yelling over the dusty roar of fellow scientists' apparatuses. Noa, Linnaea, Pietro, David, and, of course, Elizabeth and Herman (the campsite was lovely, yes?), thank you for being in my corner.

Anika L. Vroom
Delft, July 2023

Preface

This thesis stems from the Ruisdael project, a project created to gain better insight into weather and how the contributing factors behave over various surface types. The Ruisdael initiative explores meteorological tools and data from three surface types in the Netherlands: Rotterdam (urban); Cabauw (field); and Loobos (forest). This thesis concerns the set-up and use of data from a Distributed Temperature Sensor (DTS) cable running vertically along the tower at the Loobos site. The instruments on this tower gather a variety of other meteorology-related measurements in addition to the DTS data. If temperature profiles and gradients can be tracked through the vegetation layer, this method could have further applications in meteorology and hydrology, such as gathering data on heat transfer over or through other types of surface covers. This particular data-gathering method would particularly benefit situations where the goal is to document spatially and temporally high-resolution data over a small surface area.

Sometimes, rather than theory, research begins with observation and curiosity. "What does it look like?" "Are there any patterns?" In this case, that curiosity started with the the high-resolution data gathered at the Loobos site. Small fluctuations could be seen in the data, which led to the question: "Can individual eddies be tracked using the temperature profiles generated with fiber optics?"

Since the circumstances under which data are analysed are vital for data comparison, the focus soon shifted to matching up the profiles and profile videos to the weather during data collection. What better way to do this than to add a third dimension, time, to the profiles? Thus, the temperature maps were created. These were filled with forms and features, which sparked a new round of curiosity, leading to an exploration into the ways in which viewing the temperature over time in this manner could provide insight into vertical temperature distribution patterns. A wavelike inversion layer revealed itself in these images, leading to the third and final round of observation and curiosity. This exploration centered on which elements of the weather might link to inversion height and strength, and how strongly.

The answers to these questions revealed themselves piecewise, and sometimes the results in one area of research shed light on what once seemed a dead end to an earlier train of thought, creating an iterative process of closing and re-opening old files and notes. Combined, all of these smaller questions and observations paint an image of what fiber optics can say about heat transfer now, and hint at what they may achieve in terms of observing heat transfer under a different set-up. The understanding gained can be implemented to build specifics into weather and climate models, yielding more accurate forecasts and predictions.

"Big whirls have little whirls
That feed on their velocity,
And little whirls have lesser whirls
And so on to viscosity."
- Lewis F. Richardson, 1920

Abstract

This thesis explores the application of Distributed Temperature Sensing (DTS) technology to observe temperature gradients and turbulent eddies within and above a forest vegetation layer. Atmospheric temperature gradients tie directly to heat transfer, a primary mode of which are turbulent eddies. The goal in studying these elements is to enhance the understanding of land-atmosphere coupling, which plays a role in climate and weather modelling. The data collection took place in the first two weeks of November 2022 at a meteorology study site in Loobos, the Veluwe. A fiber optic cable was installed, running from the forest floor to 1.5 times the canopy height along a tower. The DTS technology provided high-resolution temperature measurements at one-second intervals. Fluctuations in these profiles could potentially be associated with turbulent eddies. By analyzing temperature profiles over time and integrating meteorological data, the study provided insights into the temporal evolution of vertical temperature distribution at the test site and its sensitivity to weather conditions. Phenomena such as direct sunlight, rainfall, canopy effects, and inversion layers were identified in the DTS data and validated with other meteorological measurements. Notably, sharp temperature inversions observed on two nights exhibited strong correlations with wind speed and its variation. Increases in wind speed and variability were associated with lower inversion heights.

Contents

1

Introduction

The movements of energy and matter within and between systems govern earth's natural processes, determining everything from what grows where, to the locations and frequency of flooding. Land and atmosphere affect each other, feeding into or breaking down the patterns that define them. As is the nature of a coupled process, this interaction is driven by and, in turn, drives the weather. Understanding land-atmosphere coupling is not only vital for present-day measures and activities (such as predicting the course and magnitude of a hurricane or determining the concentrations of air pollutants in urban spaces), but also imperative for future preparedness; climate projection models rely on simplifying and coding these coupled systems.

Although most of humanity dwells at plant level, and forests make up just a little under a third of global land-surface covers (FAO, 2020), land-atmosphere coupling in and above the vegetation layer is not yet comprehended in detail, and, as such, features in a wide range of studies and research. One reason for this lack of understanding is that vegetation itself plays a crucial role in determining regional evaporation, radiation, and precipitation, among other factors, adding complexity to the system (Green et al., 2017; Moene & Dam, 2014). Another reason this coupling is difficult to capture numerically is due to land-vegetation-atmosphere feedback loops, which are hard to identify, partially due to challenges in measuring fluxes, and in turn typically underrepresented in earth system models (Green et al., 2017). Current theory on the various processes and modes of transport involved in land-atmosphere coupling through and above a vegetation layer, as well as their observation, are studied and described in detail in textbooks like *Transport in the Atmosphere-Vegetation-Soil Continuum* by Moene & Dam (2014) or the *Springer Handbook of Atmospheric Measurements* by Foken (2021), as well as a variety of papers (da Rocha et al., 2004; Oliphant et al., 2004; Meier & Scherer, 2012; Puma et al., 2013; Euser et al., 2014; Williams & Torn, 2015; Green et al., 2017; Schilperoort et al., 2020; Butterworth et al., 2021; Peltola et al., 2021).

While the complexity of land-atmosphere coupling with a vegetation layer causes many research gaps, many patterns and relationships have been documented to date. Forests play a large role in the transport of moisture from the ground into the atmosphere via transpiration (Green et al., 2017; Williams & Torn, 2015). For this metric, leaf area is of particular importance (Puma et al., 2013), indicating that the transpiration rate varies seasonally. Heat flux is disguised in the transport of moisture, as water vapor releases energy into the atmosphere when it goes from a gaseous to a liquid state (Moene & Dam, 2014). Next to this latent heat flux, sensible heat flux (the movement of temperature, or heat that can be "sensed") also plays a role in land-atmosphere coupling. Above a primarily homogeneous surface such as a field, this flux can be estimated based on the wind velocity and temperature observations at two heights (Thomas et al., 2012). Forests, on the other hand, complicate this process, as the canopy can act as a “blocking layer”, decoupling the processes that occur below and above the tree foliage and resulting in different temperature gradients above and below the canopy (Schilperoort et al., 2020). Sharp temperature inversions, a warm layer of air residing on top of a colder layer, may or may not accompany this decoupling. In the recent study of Schilperoort et al. (2022), these sharp inversions were discovered in a forest on clear nights with low wind speeds, and exhibited wavelike oscillations.

Heat transfer between the land surface and the atmosphere is a widely studied phenomenon in environmental science as it plays a key role in understanding and predicting the weather, as well as generating projections of what the future climate might be like (Butterworth et al., 2021; Foken, 2021). Sensible and latent heat fluxes at an interface are often compared in the form of the Bowen ratio ($B = \frac{SHF}{LHF}$). Forests have a higher Bowen ratio in dry months, indicating that they hold onto moisture well, thus decreasing latent heat transfer and potential rainfall (Moene & Dam, 2014; da Rocha et al., 2004). The seasonal growth cycles of (specifically deciduous) forests also affect the Bowen ratio; the full foliage of late spring allows for much more transpiration, lowering the Bowen ratio as compared to winter. Thus the energy balance in forests changes throughout the year as trees grow and lose their leaves (da Rocha et al., 2004).

Trees also directly absorb heat during the day and release it after sundown, providing not only a heat storage function, but also potentially leading to air movement as a temperature difference is generated between the trees’ surfaces and atmosphere (Moene & Dam, 2014; Oliphant et al., 2004). The morphological characteristics of forests also affect these transports, as trees possess a large aerodynamic roughness, affecting wind flow and thus the movement of mass and heat (Moene & Dam, 2014). However, even in the roughness sublayer above forests, one way to bypass these challenges and estimate sensible and latent heat fluxes is through monitoring the motion of turbulent eddies coupled with humidity data (Katul et al., 1996). Another way to approximate these fluxes is by linking them to temperature and moisture gradients, as gradients drive diffusion (Moene & Dam, 2014).

Atmospheric and much other outdoor research is further complicated since the conditions, which should be held constant for gathering and comparing data, are unique and cannot be regulated or re-created. This uncontrollability means that improving observation technologies and methods plays an essential role in atmospheric research, as they allow scientists to better select and compare similar sets of data (Foken et al., 2021). Part of the reason it is difficult to learn more about the exchange of heat and moisture between the land and atmosphere is the mismatch between instrument measuring methods and what needs to be measured. To obtain a proper view of the transport modes of heat and moisture in, under, through, and above the vegetation layer, spatially and temporally detailed information is needed. Current measurement methods mainly consist of (combinations of) point measurement systems, which are detailed but not spatially insightful, and remote sensing techniques, which lack detail but provide spatial range (Thomas & Selker, 2021). A relatively young method of measuring temperature, the Distributed Temperature Sensor (DTS), might provide a solution to this instrument deficiency.

The DTS functions by sending a laser through a single fiber optic strand, then measuring the backscattered signal to determine the temperature (Ukil et al., 2012; Thomas & Selker, 2021). This process allows for data gathering at many points and in quick succession, providing a high spatial and temporal resolution. Specifically when combined with other instruments, the DTS shows promise in its ability to observe temperature gradients and heat and moisture fluxes over both non-forested (Hilland et al., 2022; Izett et al., 2019; Thomas et al., 2012) and forested areas (Schilperoort et al., 2018, 2020; Peltola et al., 2021, 2022; Schilperoort et al., 2022).

1.1. Research Aim

This research project aims to provide more insight into heat transfer through and above a forest vegetation layer by testing how well the DTS can observe heat transfer, as monitoring and better understanding this layer can help improve and evaluate climate and weather models. This research looks primarily into temperature profiles and turbulence from the forest floor to over 1.5 times the canopy height. To do so, a DTS measurement system was constructed in Loobos in the Veluwe to gather data. This thesis addresses the question:

"To what extent can turbulent eddies and temperature gradients in a forest be identified using fiber optic sensors?"

The following sub-questions break down the main question into three focus areas:

- To what extent are individual turbulent heat transfer eddies recognizable in the data collected by the DTS?
- What is the influence of different meteorological conditions on the vertical distribution of temperature over time?
- What influences the inversion height throughout the canopy?

2

Background

2.1. Heat Transfer and Temperature Gradients

The diurnal cycle and resulting turbulent motions drive heat transfer between the land and atmosphere, influencing the structure of the atmosphere in the process. The energy balance over the land surface and the fluxes involved can be calculated by quantifying and comparing the modes of energy and mass transfer. Some of these fluxes are strongly linked to the temperature and moisture gradients present in the atmosphere. Forests possess a combination of qualities unique to the surface cover type, which should be taken into account when working to understand the causes and effects of heat exchange in, under, and through the canopy.

2.1.1. Atmospheric Boundary Layer

The lowest portion of the troposphere, known as the Atmospheric Boundary Layer (ABL) is partially governed by turbulence. This region of the atmosphere is of particular interest as it is directly influenced by the Earth's surface and, as such, the portion of the atmosphere we interact with most (Foken, 2021). When performing calculations on turbulent processes (of which heat exchange is one) many simplifications are performed so that the calculations become manageable (Hilland et al., 2022). Better understanding and studying these processes on a small scale can improve the larger scale process calculations.

At night, the ABL is generally only 100m-200m thick in most places; the air is stably stratified, with the lower layers having a lower potential temperature than those above (the concept of potential temperature is further explained in Section 2.1.2 - Turbulence and Eddies). A typical positive, stable, night time potential temperature gradient is shown in Figure 2.1. During the day, the ground surface is heated through solar radiation, which leads to instability in the form of a negative potential temperature gradient as the air directly above the ground surface becomes warmer, and thus less dense than the air above it. This instability, displayed in Figure 2.1, results in plumes of warmer air and turbulence as the air mixes and moves, growing the ABL to a couple of kilometers and leading to a more uniform distribution of temperature (Kleissl & Garai, 2011; Moene & Dam, 2014). Both the night and the daytime ABLs are capped by an entrainment zone, which typically features a strong temperature inversion, along with strong gradients in wind and moisture (Foken, 2021). Reality is massively more complex than this description, as these patterns only describe some of the general mechanics of how heat is transferred, and everything from the topography, to the surface cover and colour, to cloud formation, to wind, to precipitation, affects the magnitude and timing of these patterns.

The inversion layer that caps the ABL is a stable region in which the potential temperature increases

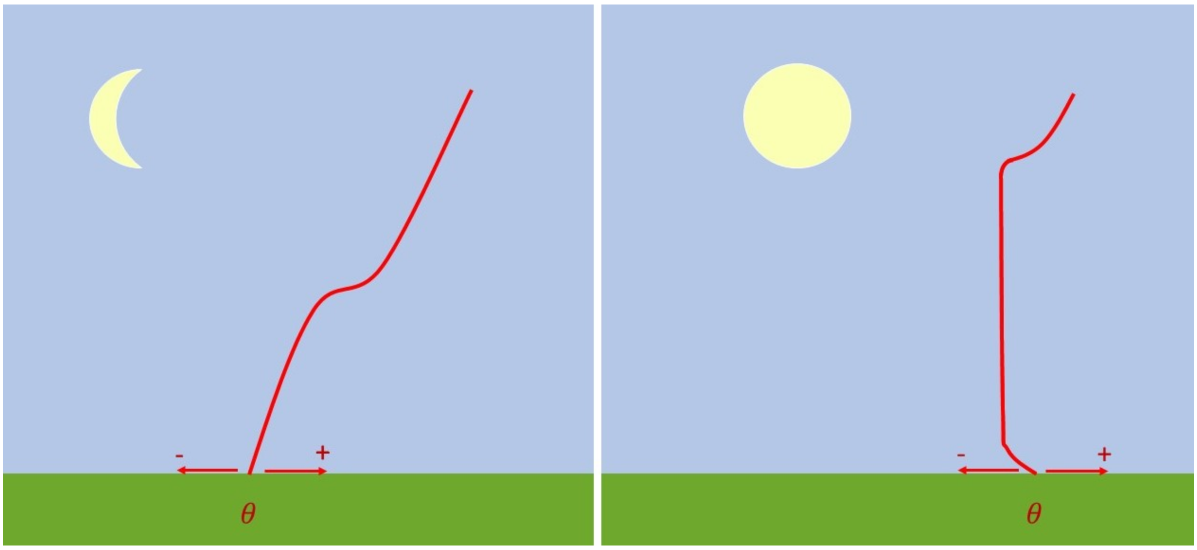

Figure 2.1: Typical potential temperature profiles for night (left) and day (right). At night, the ABL is stable and capped by inversion at the entrainment zone. Daytime ABLs are thicker and capped by a similar inversion later.

with height. This increase in temperature means that the air lower in the layer is denser than the air above, and therefore the inversion acts as a capping layer, blocking exchange between the ABL and the free troposphere (Foken, 2021; Moene & Dam, 2014). Next to this inversion layer, temperature inversions also take place within the ABL; depending on the strength of the inversion, these then limit the exchange of air (and thus heat, moisture, pollen, pollutants, and other particles) between the area above and the area below the inversion.

2.1.2. Mechanics

Energy can be transferred by conduction, convection, and radiation. Conduction has to do with a transfer of kinetic energy (systems involved are not physically exchanged or moved, but must come into contact with each other), while convection is tied to a physical transport of mass that contains a certain energy. Radiative heat transfer occurs when electromagnetic radiation is released, decreasing the energy of the system that does so and increasing the energy of the system that absorbs it (Lienhard IV & Lienhard V, 2020; Moene & Dam, 2014).

Energy Balance

The energy balance at the earth's surface indicates which variables play a role in the transfer of energy between the land and atmosphere. Considering a control volume including soil, air, and vegetation, the energy balance can be described by the equation:

$$Q^* - H - L_\mathrm{v}E - G = \Delta S_{ha} + \Delta S_{hv} + \Delta S_{hs} + \Delta S_{lat}, \tag{2.1}$$

where Q^* is the net radiation, H the sensible heat flux, $L_\mathrm{v}E$ the latent heat flux, G the ground heat flux, and the ΔS terms represent storage of sensible heat in the air (ΔS_{ha}), vegetation (ΔS_{hv}), soil (ΔS_{hs}), and storage of latent heat (ΔS_{lat}) (Moene & Dam, 2014). Here, Q^* covers the change in energy due to radiation. The sensible heat flux refers to a change in energy due to a change in air temperature (it can be "sensed"), while the latent heat flux (where L_v refers to the latent heat of vapourization) is the change in energy due to the transfer of particles that have a different phase. The prime example of latent heat flux in the atmosphere is evaporation and the movement of water vapour, which holds the potential to release energy when it turns into rain. Both sensible and latent heat fluxes are examples of convection (though some sensible heat flux is bound to occur through conduction), while the ground heat flux is a conductive term (Moene & Dam, 2014). In the case of the in and outputs balancing out, such that the left hand side of Equation 2.1 equals zero, there is no net exchange of energy between the control volume and the system surrounding it.

Turbulence and Eddies

A primary mode of convection, turbulence plays a key role in the transfer of moisture, gasses, momentum, and heat throughout the atmosphere, which, in turn, determines the weather (Foken et al., 2021; Moene & Dam, 2014). Molecular and turbulent diffusion both work to disperse gradients in the potential temperature. Turbulence works on a much larger scale than molecular diffusivity and, as such, is responsible for more of the heat transfer in the atmosphere (Moene & Dam, 2014).

The lowest part (roughly 10%) of the ABL, also known as the surface layer (SL), is often assumed to have a constant turbulent flux, except in the case of buildings and tall vegetation. For forests, there is less turbulent exchange under the canopy, and relatively more from right above the canopy to twice the canopy height (Foken, 2021). In contrast, when unhindered, the turbulent exchange of hot and cold air often forms a rolling 3D structure of cells, also known as eddies (Kleissl & Garai, 2011). These eddies tend to be larger higher up, then dissipate into smaller and smaller rolls towards the ground surface (Moene & Dam, 2014). While there are many factors that affect how heat exchange looks, such as the scale of the area of interest and the season and seasonality (Butterworth et al., 2021), the main drivers of this process are wind shear and surface heating (Moene & Dam, 2014).

Turbulence can be broken down into air parcel movements, the vertical component of which depends on the buoyancy, and can be found by examining temperature fluctuations. These fluctuations lead to a differing density of an air parcel from its surroundings, which drives parcel movement. When comparing the temperature of a parcel to the average air temperature, the moisture and elevation both play key roles. A higher humidity (if all other variables are maintained) raises the buoyancy of a parcel, as water vapour is less dense than the average mixture of gases in dry air. If two parcels located at different elevations hold a similar moisture content and measured temperature, the one at a higher elevation holds more heat (Moene & Dam, 2014). As such, temperatures at different elevations can be compared by translating them into potential temperature:

$$\theta' = T(\frac{P_{ref}}{P_{at_h}})^{\frac{R}{c_p}}, \tag{2.2}$$

where θ' is the potential temperature of the air parcel, T is the absolute temperature, P_{ref} is the reference pressure (often selected as 1000 hPa or the pressure at the ground surface), P_{at_h} is the pressure at the altitude of measurement, R is the specific gas constant, and c_p is the specific heat of the air at a constant pressure, (Moene & Dam, 2014; Foken, 2021).

Turbulence links back to heat flux as described by Equation 2.3; the turbulent sensible heat flux over a given time period is based off of the movement of air over that same time interval.

$$H = \overline{\rho} c_p \overline{w'\theta'}, \tag{2.3}$$

where $\overline{\rho}$ is the average air density, and $\overline{w'\theta'}$ is the turbulent kinematic flux (w is the term for vertical wind speed and θ for potential temperature, the overbar and primes indicate the covariance of the two) (Moene & Dam, 2014). The turbulent latent heat flux can be found in a similar manner, substituting moisture for temperature. In this way, turbulent transport in the atmosphere determines two of the terms (H and L_vE) in the surface energy balance described by Equation 2.1.

Whether or not and to what magnitude turbulence occurs depends on the temperature gradient (along with other factors, such as wind speed). A stable profile will work against turbulent transport, while an unstable one will encourage it, increasing heat transfer via turbulence. Vertical gradients can be linked to vertical fluxes, which, with the correct additional information, can then be implemented to estimate the heat transfer of a given scenario (Moene & Dam, 2014).

According to Peltola et al. (2022), the turbulent sensible and latent heat fluxes are directly proportional to the mean temperature gradient, and the turbulent sensible heat flux can be calculated with this gradient in combination with the vertical wind speed and how far air is displaced. In this way, gradients coupled with wind speed data can be used to estimate turbulent fluxes.

2.1.3. Forests

In forested landscapes, unevenly distributed areas of shade and sun are present. The shape, location, and distribution of these areas heavily depend on factors such as the season, tree-type, and cloud cover. In a deciduous forest, the upper trunks and canopy can be exposed to sunlight while large swaths of forest floor are not during summer, while the forest floor will experience little shade on clear winter days. The patterns of shade and sun, along with the thermal, reflective, and life-related properties of forests, affects heat transfer below the canopy.

Forests bear a temperature profile pattern that differs from that of a non-forested surface. During the day, the warmest temperature will be where there is a maximum absorption of radiation, and thus where the leaf density is highest. Below this point, the air is stably stratified. At night, the ground and trunks release the heat they have absorbed, causing maximum cooling where there is a lot of foliage, leading to some instability and turbulence (Moene & Dam, 2014). While the canopy faces the most heating due to the interception of shortwave radiation, it is also a site of cooling, due to transpiration and radiation (Meier & Scherer, 2012). Once again, this is a description of average behaviour, rather than a strict set of rules.

The air in and above a forest can also experience decoupling (Schilperoort et al., 2020), which is sometimes indicated by a temperature inversion (Schilperoort et al., 2022). In Schilperoort et al. (2022), inversions were found in a forest on clear nights with low wind speeds.

The various properties of forests differ from other surfaces, which will affect radiation and heat storage, and thus the heat transfer, present (Butterworth et al., 2021; Moene & Dam, 2014). For example, forests tend to have a higher emissivity than urban regions (and a slightly higher one than grasslands), affecting the radiative balance by better absorbing and releasing energy. Other key properties that differ by surface cover type are albedo, aerodynamic roughness, and Bowen ratio (which also depends external factors e.g., weather). Another important quality that sets forests apart is the ability to store heat in both biomass (foliage, branches, trunks, the forest floor) and the canopy air-space. This storage of heat plays a key role in the temperature distribution as described by Moene & Dam (2014), and the amount of storage shifts throughout the diurnal cycle, as well as seasonally (Oliphant et al., 2004).

Next to their material and morphological characteristics, trees are also life forms, and some of their functions interact with and affect heat transfer both above, within, and under the canopy (Butterworth et al., 2021; Green et al., 2017). The stomata of plants react to factors like radiation, temperature, atmospheric vapour deficit, external and internal CO_2 concentration, and leaf water potential. Trees have a strong effect on the latent heat flux as they can take water from much lower in the ground than would be accessible via evaporation from the ground surface, meaning that, depending on the factors listed above, trees can affect the latent heat flux in and above the canopy (Moene & Dam, 2014). Shrubs and smaller plants create a similar effect in the understory.

2.2. DTS

Distributed Temperature Sensors use optical fibers to detect the temperature along a cable based on the backscattering of light. They do so by measuring and comparing Stokes and Anti-Stokes Raman (inelastic) backscattering (Ukil et al., 2012). This provides accurate, high-resolution data of strain and temperature, which have a range of applications, including, but most certainly not limited to, wind speed measurement, humidity sensing, pipe monitoring, and locating fires (Ukil et al., 2012; Zhang & Jin, 2019). One of the pros of measuring using DTS is that temperature profiles can be created and gradients calculated, such as the profiles needed for meteorology-related predictions and calculations. These profiles will have relatively little error since they are all made using the same cable, rather than discrete measurement devices, and since the distance between measurements can be made relatively small depending on device settings (Schilperoort et al., 2018).

The DTS is useful for measuring in a forest because the high accuracy allows for detection of the small temperature gradients found there (Schilperoort et al., 2018; Izett et al., 2019). Peltola et al. (2021) studied the ability of the DTS to observe and quantify air flows in a forest (considered complex due to the high aerodynamic roughness) based on DTS data, and found that it provided insight into mixing processes and flows. The DTS data alone lacked accuracy as compared to the sonic anemometer data, but provided more spatial insight than the point measurements.

Next to temperature measurement, one of the common applications of the DTS in environmental science is to wrap wet cotton around a cable to measure the wet bulb temperature. The temperature and wet bulb temperature can be used to calculate the relative humidity and the Bowen Ratio, an important element for understanding water and heat fluxes and land-atmosphere energy exchanges (Euser et al., 2014; Schilperoort et al., 2018). In a similar fashion, the cables can also be heated to measure the wind speed (referred to as Actively Heated Fiber Optics, or AHFO) (van Ramshorst et al., 2020).

3

Materials and Methods

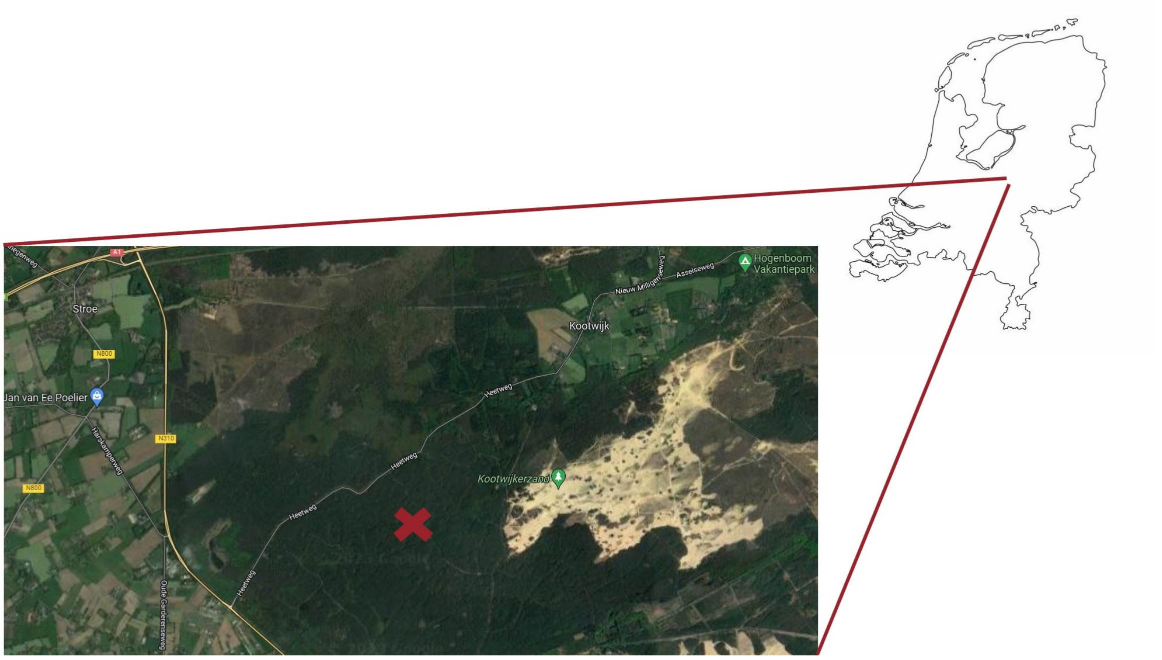

Figure 3.1: The location of the study site in the Veluwe (Google, n.d.).

3.1. Site

The study site resides in Loobos, in the Veluwe, slightly south of Kootwijk, at coordinates 52.166446, 5.743554 (see Figure 3.1). This forest consists of well-spaced, sparsely-branched evergreens (*Pinus sylvestris*, more commonly known as Scots Pine) on a sandy soil, growing to a canopy with a height of about 18 - 22 m that lets some direct light through to the understory and forest floor (see Figure 3.2). Smaller deciduous trees and shrubs also grow there, bare of leaves throughout this study, which took place from October 30th through November 17th of 2022.

The long-term average yearly temperature on-site is 10.3 °C, with warm summers, cold winters, and an average yearly rainfall of 900 mm/year, with more wet days than dry. November is significantly colder, averaging about 6.5 °C, with highs averaging 9.5°C and lows 3.5°C. The average rainfall is about 80 mm over the month with 8-10 dry days. The average wind speed is 3.5 m/s on a yearly basis, with the colder months averaging slightly higher than the warmer ones (*Klimaatviewer*, n.d.).

Figure 3.2: The sparse canopy in Loobos allows sunlight through to the forest floor.

3.2. Materials and Set-up

There is a tower on-site used for meteorological data collection with a wide range of instruments, shown in Figure 3.3a. These instruments measure variables including eddy covariance, temperature, long and shortwave radiation, wind speed and direction, and relative humidity. This tower also hosts fiber-optic cables, used by the DTS to measure temperature.

The DTS on-site is a Silixa Ultima M. The fiber is Kevlar-reinforced and about 200 m long, the coating increases the cable thickness to a 1.6 mm diameter. To calibrate the temperatures read from the fiber, two calibration baths with an isolating foam inlay were used. The tower is 36 m tall to the highest platform, the cable extends along the northeastern face of the tower (off the northern corner) to a height of just over 37 m. At the top, the cable is led through a PVC bend of about 1.3 m in length, as displayed in Figure 3.3b. One side of the cable is encased in a sock of cotton (this is for the purpose of measuring the wet bulb temperature, these data are not used in this study), the other is bare to the elements, except where it is protected by a sun screen in and above the canopy (displayed in Figure 3.3c). This sun screen was constructed out of thin mesh to prevent a measurement error due to solar radiation (Schilperoort et al. (2018) found that direct sunlight can raise the temperature perceived by the DTS by up to 3 K). Both the fiber and the sun screen were suspended off the side of the tower using metal arms and plastic brackets (3.3d). In places where the fiber needed to be attached to objects or held in place, foam was used to avoid creating sharp angles or possible breaking points.

(a) The measurement tower in Loobos.

(b) At the top of the tower, the fiber is led through a bend made of PVC and padded with foam.

(c) The sun screen (gray mesh) around the bare cable and the cable with a cotton sock run parallel to each other up the side of the tower.

(d) The metal arms hold the wet fiber (outer) at 0.90 m from the tower, and the dry fiber (inner) at 0.45 m from the tower. The lower levels of the tower (up to 20 m) have an additional support column at 0.35 m from the platform edges.

(e) The two calibration baths are stacked upon each other, the upper heated with a motor and the lower kept relatively cool at ground temperature.

(f) The PVC pipe at the base of the tower.

Figure 3.3: Various images of the DTS set-up at Loobos.

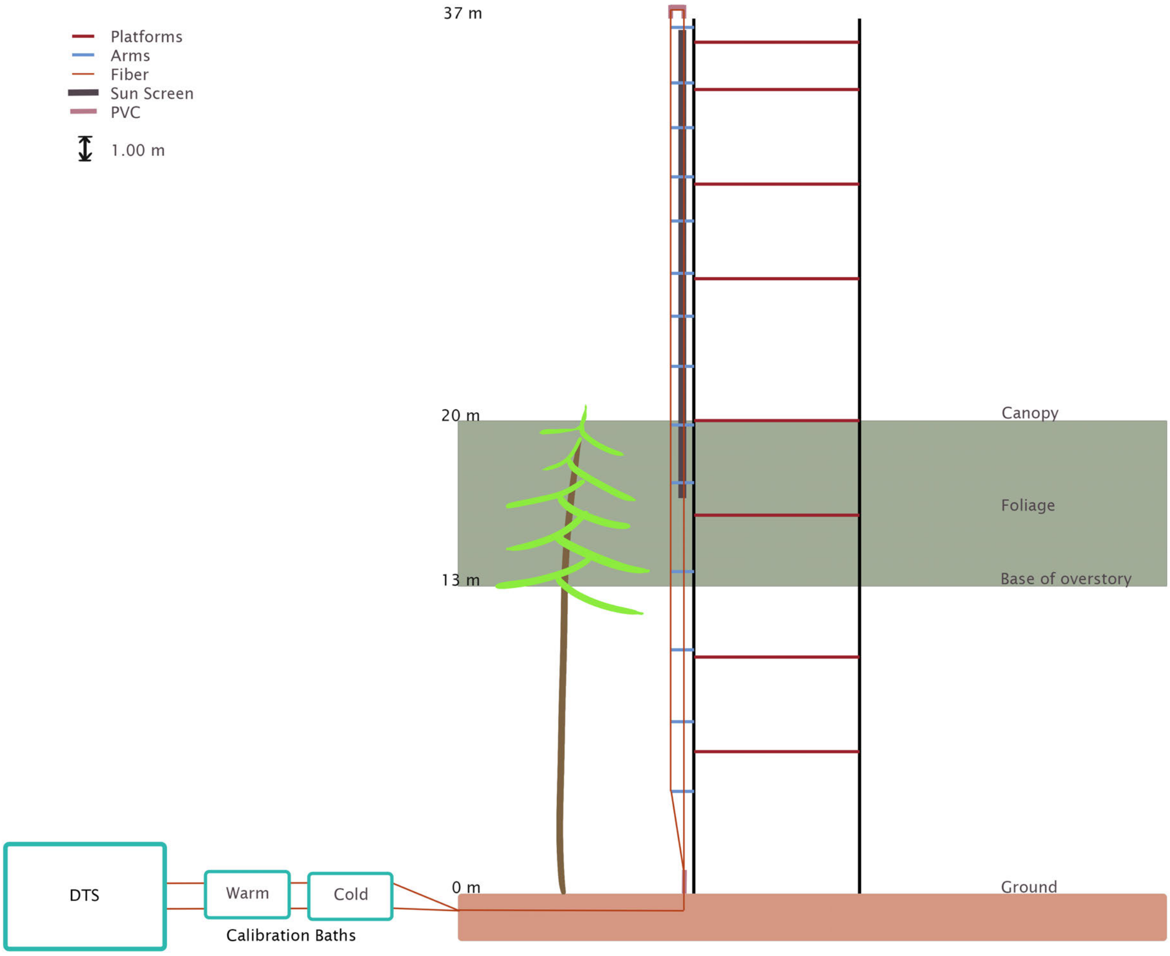

Figure 3.4: Schematic drawing of the tower and DTS set-up. The fiber runs from the DTS through two calibration baths, under the ground, along the tower to the top, then back down, through the baths to the DTS again. The fiber measures temperature along the length of the tower. The first meter of the fiber is encased in PVC. The sun screen runs from the upper portion of the overstory to 36.8 m. There is little foliage under the start of the overstory, which commences at about 13 m and ends at about 20 m.

As displayed in Figure 3.4, the DTS hooks up to a single fiber-optic cable in a double-ended setup. The cable goes through two calibration baths on both ends. One of the baths is heated using a motor, the other is left to match the ground temperature (see Figure 3.3e). The cable is run from the baths through an underground PVC pipe, and then up from the base of the tower to the top and back down again. In Figure 3.3f the base of the cable is displayed; the first 1.00 m of the cable is protected by a PVC pipe.

3.2.1. Meteorological Data

Data obtained from both the KNMI (*KNMI - Uurgegevens van het weer in Nederland*, n.d.) and the Ruisdael Loobos tower (*Site Loobos*, n.d.) illustrated the weather conditions under which the DTS data were generated. Longwave and shortwave data gathered at 20 second intervals and 38.2 m height in Loobos using a Kipp&Zonen CM21 Pyranometer, CG1 Pyrgeometer, and PT100 temperature probe were processed and added (the longwave radiation values were adjusted for the emissions of the measuring device). Hourly rainfall data was obtained from the nearest KNMI rain-measuring site in Deelen, about 15 km to the south-southeast of the tower. Temperature and horizontal wind speed data from the Loobos tower for heights 38.2 m, 22.1 m, 15.7 m, and 7.4 m, gathered at 20 second intervals with Vaisala HMP35A Platinum resistance thermometers, Vector Instruments A101ML Cup anemometers, and a Vector Instruments W200P Wind vane were also utilized (*Site Loobos*, n.d.).

3.3. Methods for Data Collection

The data studied was gathered every 0.256 m along the fiber, over a time interval of 1 second. To reduce measurement error, a double-ended set-up was implemented (Thomas & Selker, 2021), so the data were gathered from both directions, with each pair of observations grouped together under one timestamp. The resulting total number of measurement moments averages to a time resolution of about 3.6 seconds. The measurement frequency was not completely uniform, so the data are unevenly distributed through time, with some data points closer to three seconds apart, and some closer to four.

To allow for calibration, two PT100 temperature probes were implemented, one in each calibration bath, and these probes and the Length Along Fiber (LAF) positions of the baths were added to the DTS settings.

3.4. Methods for Data Analysis

The overall goal of the data analysis was to examine the temperature profiles for signs of heat exchange, see if that heat exchange could be characterized, and better understand the temperature distribution in the forest. To do this, the data had to first be calibrated, as explained in Section 3.4.1.

Temperature profiles were then generated from these data for select conditions (see Section 3.4.2), which functioned to indicate the stability at a given moment (or averaged over a given time interval), for the vertical column of air surrounding the fiber. These profiles were then examined for signs of turbulent heat transfer, the methods for which are further explained in Section 3.4.3.

To better understand how the temperature changed over time, these data were also visualized as temperature over height through time (see Section 3.4.4). To better analyse the various phenomena displayed in this second main method of data analysis, meteorological data for radiation, temperature, rainfall, and wind speed were added to these plots. One of the elements visible in these "temperature maps," inversion layers, were analysed by quantifying the heights and magnitudes of the inversion. As a final analytical step, the correlations between meteorological data and inversion height were explored.

3.4.1. Data Calibration and Processing

The DTS does a fair job of temperature estimation based on the ratio of Stokes and Anti-Stokes backscattering, however, a more accurate measurement can be reached by post-processing. To calibrate the raw data, the files containing the temperature probe data, Stokes and Anti-Stokes signal strengths, LAF, and timestamp were run through the open-source DTS calibration package ("dtscallibration") created and explained by des Tombe et al. (2020). These files were processed using a python script that implements the aforementioned package and the Delft Blue supercomputer. The clock used for both the DTS and the temperature probes was one hour off, so the data had to be shifted one hour forward (in this case this occurred post-calibration) for the timestamps to properly represent the local time (CET).

The measured temperature was converted to potential temperature using Equation 2.2, from here on out referred to as simply "temperature". The calibrated data was then further analysed by creating temperature profiles, and profiles of temperature deviation from the mean. The LAF was converted to height, and the dry fiber section from 1.0 m above the ground surface (so from the mouth of the PVC pipe) to 37.0 m (just before the PVC bend at the top) was isolated. These profiles were lined up with surrounding features of interest (platforms, attachment points to the tower, canopy height) and examined for patterns of hot or cold air movement.

3.4.2. Selection of Conditions

Temperature profiles for specific conditions of interest were generated, as examining data on different types of weather allows for better understanding of these weather types, and what the differences might be between them. For all conditions, a low wind speed was sought, since, if a horizontal wind speed component dominates, the potential eddies are more likely to be moved out of the vertical line of air measured. The conditions selected were:

- Low wind speed, night, clear
- Low wind speed, day, clear
- Low wind speed, night, cloudy
- Low wind speed, day, cloudy

Other profiles examined for comparison were:

- High wind speed, night, cloudy
- High wind speed, day, cloudy
- Rainy

3.4.3. Individual Eddy Tracking

Isolating turbulence in the temperature profiles by setting aside warm and cold patches not due to turbulent air motions helps to better identify eddy characteristics. One way to (partially) remove these non-eddy-related features is to examine the fluctuations from the mean temperature. Since the temperature profile changes throughout the day, this can be done with a rolling average. As the rolling average is performed over larger time intervals, each individual profile holds less weight, and so eddies are less likely to be included in the average profile. As the time interval decreases, the effects of changes in the average air temperature will be better included in the average profile, so these changes are less likely to be falsely attributed to turbulence (e.g., general warming of the air as the sun rises will not be graphed as a fluctuation from the mean, but rather incorporated into the average temperature profile for that timestamp). To determine an appropriate time interval over which to average, rolling averages over 30 seconds, 1 minute, 5 minutes, and 10 minutes were implemented.

The profiles of differences from the average temperature were generated using the rolling averages. These were then examined image-by-image, as well as in video format, to see if eddy magnitudes and movement could be detected for the various weather scenarios.

To differentiate the signals detected in these profiles from noise, noise levels in the data and the resulting error propagation were quantified and taken into account. The noise level of the data was identified using the calibration baths, since these should maintain a constant temperature. The standard deviation of the data obtained from the cold baths ranged between 0.116 - 0.119 K, and 0.120 - 0.125 K for the warm baths. The standard deviation for the data set comprised of all calibration points (σ_{all}) was calculated using Equation 3.1. Since the set-up is double-ended, and measurements are taken from both ends, each bath had two sets of data points: one measured in the "forward direction", the other in the "backward direction". Each standard deviation was weighted relative to the number of points in the bath (i.e., w_{b1fw}, w_{b1bw}, w_{b2fw}, w_{b2bw}). The variance between time steps of the standard deviations for the data set was negligible (0.000036 K^2), so this standard deviation was treated as representative for all time steps.

$$\sigma_{all} = \sigma_{b1fw} * w_{b1fw} + \sigma_{b1bw} * w_{b1bw} + \sigma_{b2fw} * w_{b2fw} + \sigma_{b2bw} * w_{b2bw}, \tag{3.1}$$

and

$$w_{b1fw} + w_{b1bw} + w_{b2fw} + w_{b2bw} = 1. \tag{3.2}$$

where σ_{b1fw} refers to the standard deviation of calibration bath 1 measured in the forward direction (the subscript "2" indicates the second bath, and the subscript "bw" corresponds to measurements made in the backward direction).

To provide insight into the magnitude of error in the data due to signal noise, the standard deviation of the noise was treated as representative of the error. To do this, the error for a single time step, e_{single}, was set equal to σ_{all}. Error propagation calculations were then used to determine the error due to signal noise in the "deviation from the average temperature" profiles. Implementing Equation 3.3 computes the error due to noise present in the rolling average profiles (e_t), where n_t represents the number of profiles combined into the average for the given time interval (t, in this case 30 seconds, 1 minute, 5 minutes, and 10 minutes).

$$e_t = \frac{e_{single}}{\sqrt{n_t}}. \tag{3.3}$$

The error of the profiles expressing deviation from the average temperature (e_{adding}) can then be found with:

$$e_{adding} = \sqrt{e_t^2 + e_{single}^2}, \tag{3.4}$$

which calculates the error when adding or subtracting two data sets, each with their own error.

3.4.4. Temperature Maps and Inversion

Another way to view the data is by graphing temperature versus time versus height, visualising the developments in temperature under, through, and above the canopy over time. The data were handled in a similar manner as described in Section 3.4.1, but, rather than generating single profiles, the temperature was expressed as colours over a specified date range. Generating additional graphs of various meteorological data helped to put the patterns displayed through this method into context.

One of the features displayed in the temperature maps, temperature inversions, were analysed by locating the height and strength of the inversion. To assess the height and strength of the inversion at each time step, the data point with the largest difference in temperature above and below said point was located. The height of this point is then the inversion height, and the difference in temperature represents the strength of the inversion. To select the window size for temperature comparison, as well as the distance between window and inversion, various options were considered. The values considered were 1.0 m, 1.5 m, and 2.0 m for window size, and a distance of 0.5 m or 0.75 m to the edge of the window. A window of 8 points (corresponding to a distance of 2 m along the fiber) and distance from inversion height to window of 2 points (0.5 m) were selected.

To further screen for inversion, a minimum average temperature difference of 0.8 K was used. As displayed in Figure A.1, no temperature screen leads to a lot of "noise" in the data points chosen, as the location with the most temperature difference might not reside at a temperature inversion (specifically if the inversion is weak or not present). Screening for too strong an inversion screens out a lot of data points that do correspond to the inversion height. This led to two data sets. For most analysis, the "screened" data were used, for some the "unscreened" data were also tested.

To explore the correlations between the inversion height and various other factors, the timestamps of the DTS data were rounded off to the nearest tenth of a second, and the meteorological data were interpolated to these timestamps using linear interpolation. This process left the DTS data almost untouched, but could significantly affect the accuracy of the meteorological data, as this added detail to the data set, expanding the data for each variable from three data points per minute to 600 data points per minute. The interpolated data that did not match with a DTS data timestamp was dropped, creating data sets of even lengths with matching timestamps. The coefficients of determination (r^2), which indicate how well one variable can predict another based on a selected model, were calculated for a line of best fit and the correlations were visualized with scatter plots. Since a linear model was used, the coefficient of determination will equal Pearson's r squared. The correlations focused on were those between the inversion parameters calculated (height and strength), and meteorological data gathered on-site. Of the variables tested, the variance and standard deviation of the wind speed were determined with rolling windows of five minutes.

4

Results

4.1. Individual Eddy Tracking

Figure 4.1 displays an example of the data processed according to the method described in Section 3.4.3. Figure 4.1a shows the deviation of the one second temperature profile from the mean temperatures, and thus the temporary fluctuations in air temperature due to turbulent eddies. These fluctuations can be compared to Figure 4.1b for information on the actual potential temperature and resulting stability.

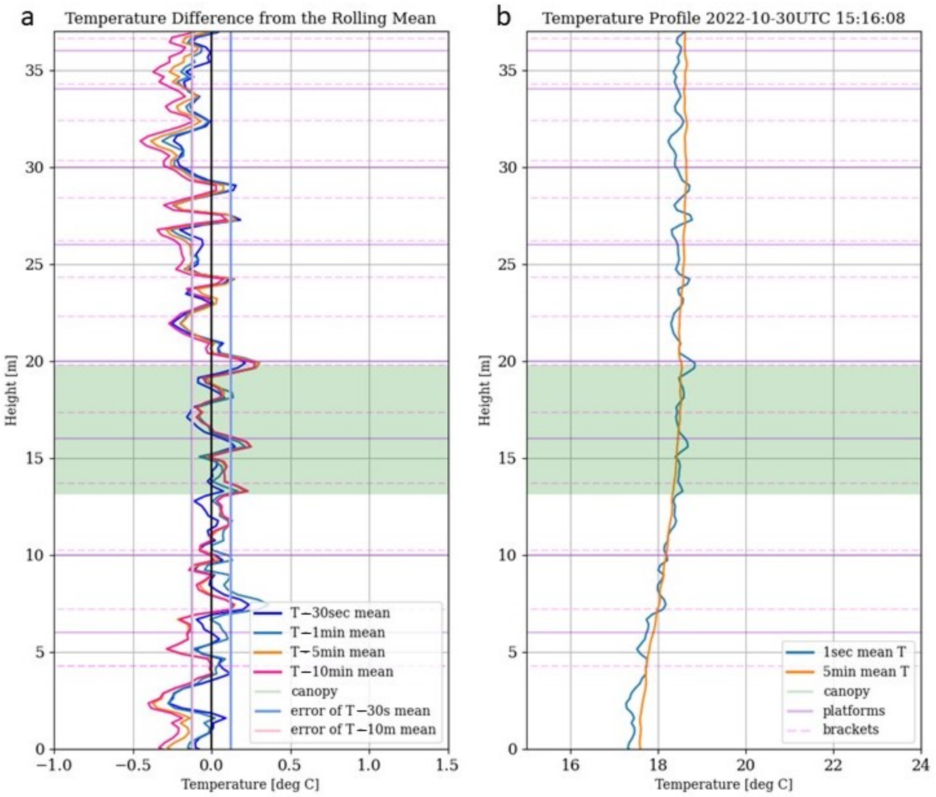

Figure 4.1: Example temperature fluctuation comparison figure. (a) Difference between the one second temperature profile and the various mean temperature profiles (e.g., "T - 30 sec mean" is the profile of the 30 sec mean temperature subtracted from the profile of the one second mean temperature). As a visual guide for determining what may be attributed to noise, the error due to signal noise is superimposed in the figure. (b) The one second mean temperature profile plotted with the five minute mean temperature profile. Tower features and the overstory are displayed in both figures.

The cold zone measured at the top of the profile in Figure 4.1 is well outside of the noise level for most measurement points, indicating that the local air parcel between 29 m - 35 m height was colder during the one second measurement period than the average air temperature for the corresponding heights. This is also reflected in Figure 4.1b, where the one second profile is colder than the air temperature averaged over five minutes, indicating an eddy of colder air at these heights. The "difference from the mean" profiles in the Figure 4.1a are all very close together in the canopy, indicating that the 30 second, one minute, five minute, and ten minute average profiles are all very similar in this zone. In contrast, the profiles spread out further above and below the canopy, therefore the average temperature profiles must be different in these zones.

These patterns, while representative of the minutes surrounding this timestamp, do not represent the data set. The profiles generated for the "typical circumstances" selected in Section 3.4.2 (not shown in this report with the exception of Figure 4.1) vary widely in characteristics. Sometimes the fluctuations are great throughout the overstory, and sometimes they remain small, such as in Figure 4.1a. No clear patterns formed in the locations and magnitude of temperature fluctuations during the observed hours. On the other hand, some (weak) patterns arose in the "difference to the mean" profile's behavior. During the periods analysed, the profiles of the difference between the one second data and the five minute and ten minute temperature data almost always displayed a similar pattern and values. The difference to the one minute average data often follows a similar pattern, but with less magnitude than the five and ten minute profiles. The profile displaying the difference to the 30 second data was the most likely to display a different pattern in the data as compared to the other three profiles. This indicates that the difference to the one minute mean might be the most appropriate metric (the incongruous shape of the difference to the 30 second mean indicates that eddies may heavily affect the mean profile, thus getting averaged out).

4.2. Distribution of Temperature

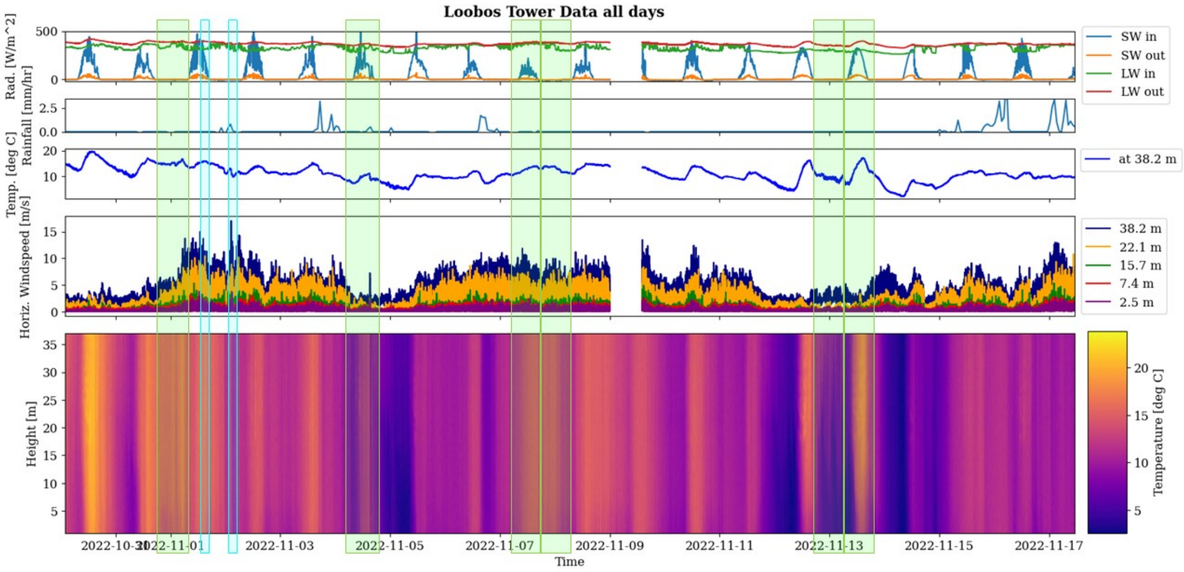

Figure 4.2: From top to bottom: radiation, rainfall, temperature at a single height, horizontal wind speed, and temperature over height data for the duration of the measurement period (October 30th 02:00 to November 17th 11:00, 2022). The days and times focused on in other figures are highlighted in boxes (green for the days and nights, and blue for additional scenarios).

The general weather for the period of study, shown in Figure 4.2, consisted of (semi)overcast days (except the 12th and 13th of November, where it cleared up) ranging between 4 °C to 22 °C with some rainfall. The wind speed fluctuated, with the coldest temperature nights falling together with lower wind speeds. The boxes surrounding certain days correspond to the data explored in more detail in the rest of this section. First, the clear, cloudy, and windy nights are analysed, followed up by the clear, cloudy, and windy days. Then, instances of sun, rain, and quickly alternating temperatures are considered.

4.2.1. Night

Figure 4.3 depicts a profile and weather data for a clear night (as indicated by the elevated incoming longwave radiation values), and low wind speeds. The temperature scale implemented in the temperature maps is unique to the temperature range so as to more clearly distinguish any features present, therefore the range in Figure 4.3 differs significantly from the overview shown in Figure 4.2. This image contains an inversion layer fluctuating between just above the canopy and 5 m above the ground, visible in both the profile and the temperature map. The profile shows a very stable atmosphere (positive temperature gradient) above the inversion height, with a roughly neutral profile (vertical) under the inversion. This indicates that, during times of inversion, exchange at and above the inversion height was limited by the temperature (and resulting density) gradient. Under the inversion height, exchange was also limited due to the lack of wind shear and near-neutral temperature gradient. The inversion layer fluctuates along with changes in wind speed, with higher, more varying wind speeds occurring as the inversion layer sinks, and less varying, lower wind speeds aligning with the higher inversion heights. This inversion layer is further analysed in Section 4.3.

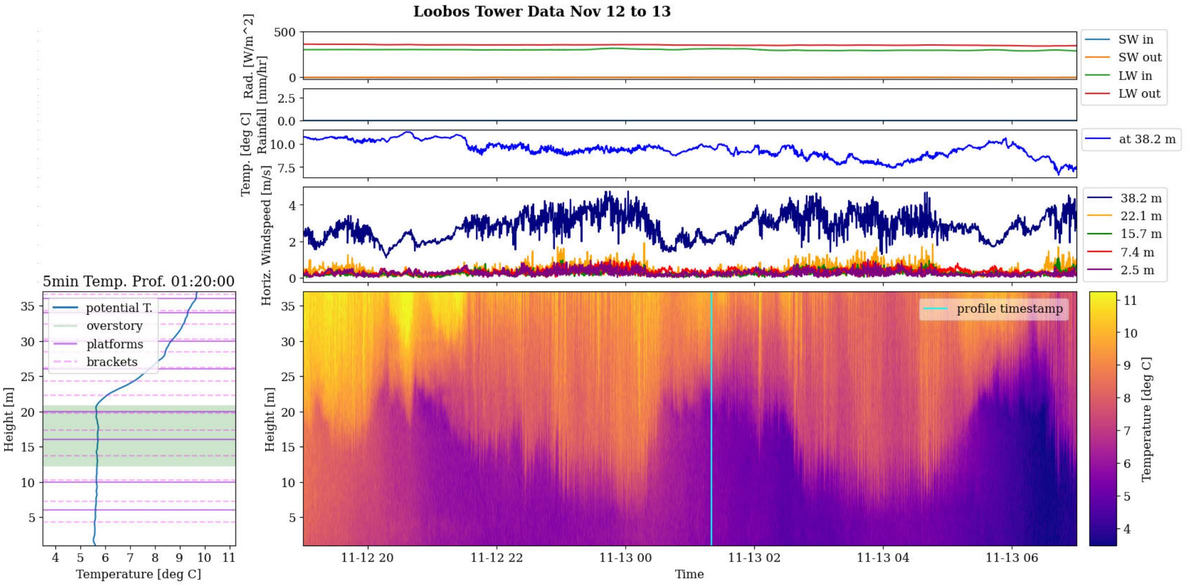

Figure 4.3: November 12th to 13th, 2022: a clear, almost windless night. The temperature profile (left) is marked on the temperature map (lower right). On the right side, from top to bottom: radiation, rainfall, temperature at a single height, horizontal wind speed, and temperature over height data for the duration of the measurement period.

The cloudy night with low wind speeds example (Figure 4.4), depicts a cold zone closest to the forest floor, and a stable atmosphere. Based on the increase in downwelling longwave radiation, the cloud cover forms around 22:00, thickening until 02:30, after which it become intermittent. While both low wind speed nights display a cold zone near the forest floor and a stable atmosphere above the canopy, the similarities do not extend much further than that. These two selected nights differ significantly in temperature range (displaying a difference of up to 10 K at some heights), this is expected since the cloud cover reflects longwave radiation back to earth, thus adding energy to the system, raising the temperature. The clear night also displayed a stronger temperature gradient, which may be directly due to the difference in temperature, since the air near the ground surface on the clear night was so much colder than the air near the top of the measurement range. The cold zone directly above the forest floor indicates that the ground temperature was likely colder than the atmosphere.

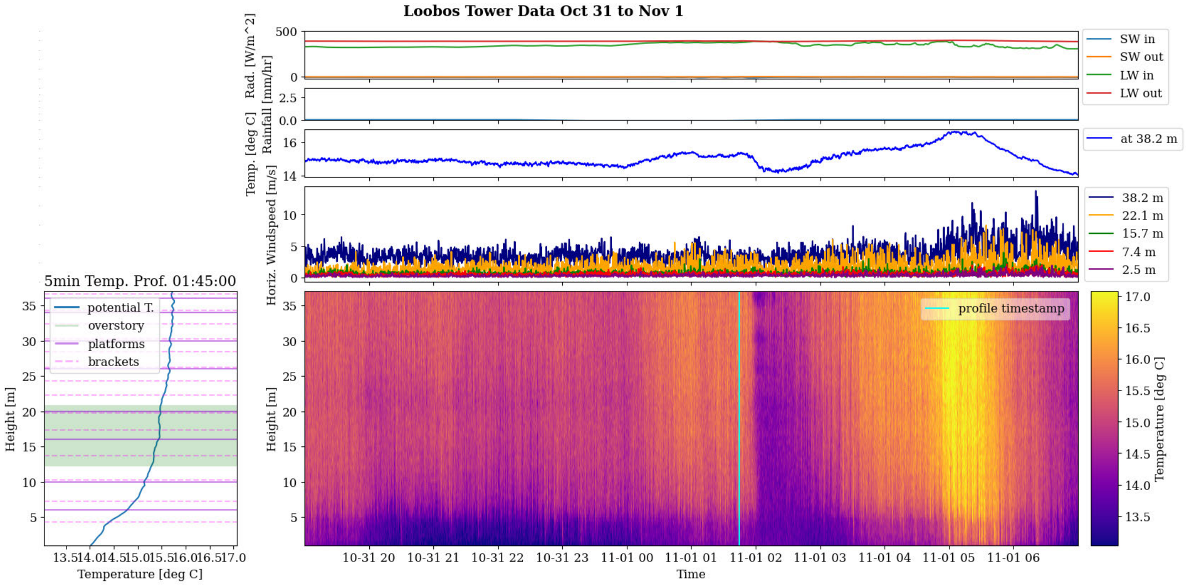

Figure 4.4: October 31st to November 1st, 2022: a mostly cloudy night with low wind speeds (barring 04:45 - 07:00). The temperature profile (left) is marked on the temperature map (lower right). On the right side, from top to bottom: radiation, rainfall, temperature at a single height, horizontal wind speed, and temperature over height data for the duration of the measurement period.

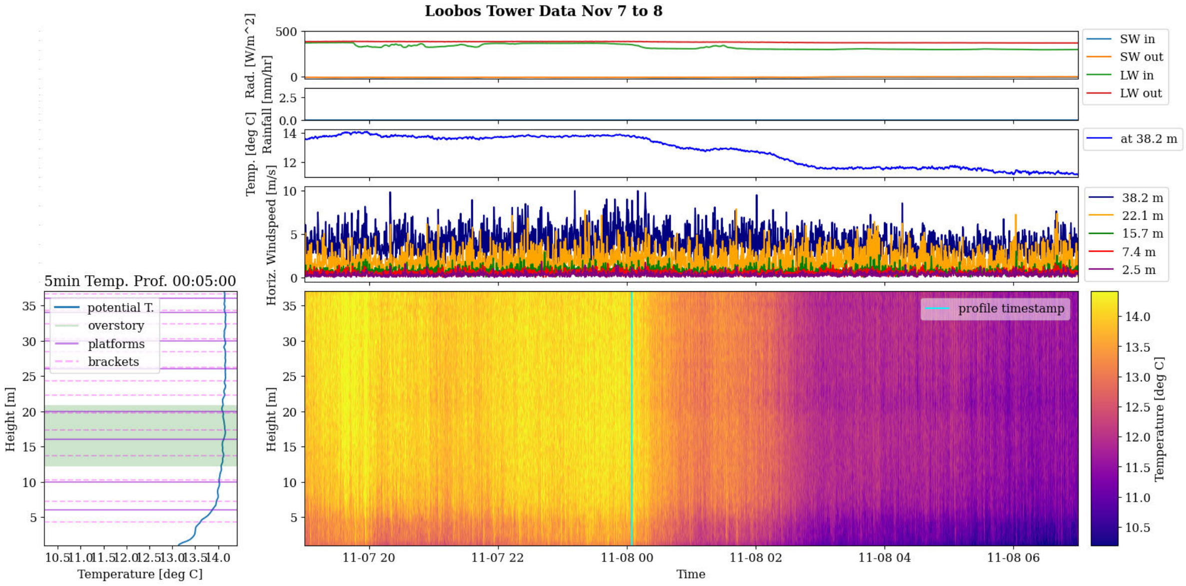

Figure 4.5: November 7th to 8th, 2022: a cloudy, windy night. The temperature profile (left) is marked on the temperature map (lower right). On the right side, from top to bottom: radiation, rainfall, temperature at a single height, horizontal wind speed, and temperature over height data for the duration of the measurement period.

While slightly lower as compared to other cloudy nights, the wind speeds on the night of October 31st were higher than the other "low wind" examples explored in this thesis. The temperature ranged only about 3.5 K over the whole evening, and the temperature map appears grainy. This difference in wind speed may have contributed to the more mixed atmosphere displayed in the cloudy night temperature map and profile (as compared to the clear night). In Figure 4.4, an increase in wind speed aligns with a warm patch (about a degree warmer than the air before and after) between 5:00 and 6:00 (well before sun-up). This may have occurred due to the wind carrying in warm air as it passed over a location with a warmer atmosphere. There is also slight visible cooling at the canopy, which may be due to transpiration (Meier & Scherer, 2012), and/or the release of of heat stored in the forest biomass (specifically at trunks, branches, and the forest floor) mentioned by Moene & Dam (2014).

The cloudy, windy night (Figure 4.5) shows a well-mixed temperature profile, and also has slightly colder zones just above the canopy and above the forest floor. This colder zone within a few meters of the canopy occurs often in the data and is usually no more than a few tenths of a degree. The temperature range over the whole night is similar to that of the other cloudy night, but with even less gradient. This lower gradient could be due to increased mixing caused by increased wind shear. The difference between this windiest, cloudy, dry night and the "low wind" alternative (Figure 4.4), is only about 1-2 m/s, which may also play a role in the similarities between the two.

4.2.2. Day

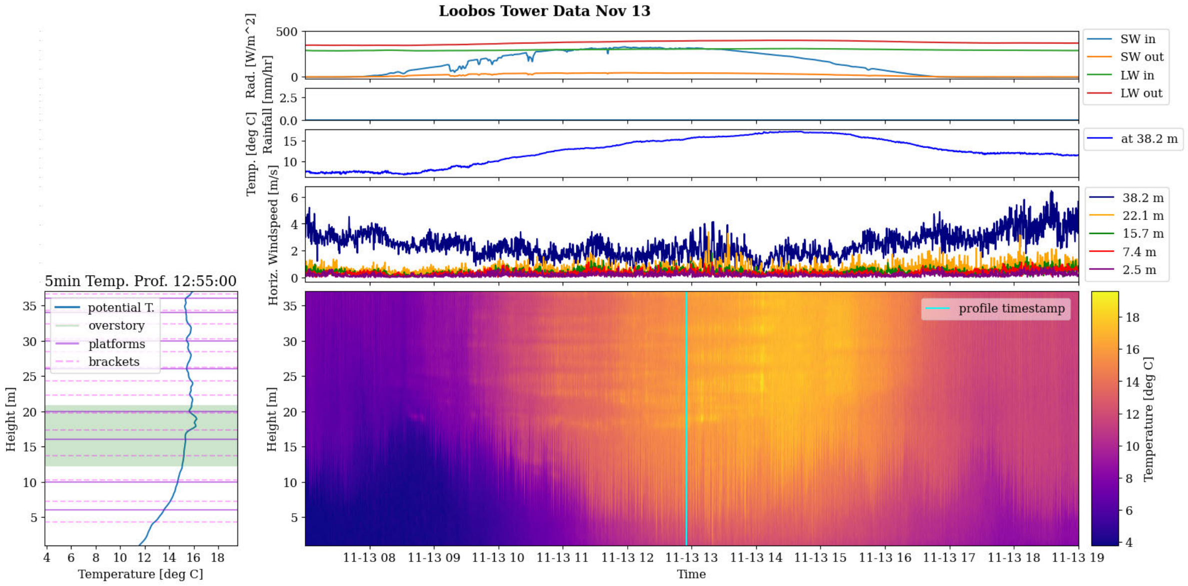

Figure 4.6: November 13th, 2022: a clear day with low wind speeds. The temperature profile (left) is marked on the temperature map (lower right). On the right side, from top to bottom: radiation, rainfall, temperature at a single height, horizontal wind speed, and temperature over height data for the duration of the measurement period.

The day following the clear night displayed in Figure 4.3, shown in Figure 4.6, also consisted of mostly clear skies with low wind speeds. A few clouds appeared in the morning, visible as dips in incoming shortwave radiation. In the figure, the temperature inversion from the night before persists, with a peak height of about 19 m around 8:00; it dips low and weakens throughout the day, and then climbs and falls in a wavelike pattern in the afternoon and evening. The alignment with wind speed observed during the preceding night appears to continue through this day to the following evening. In contrast to the clear night, the clear day profile shows a stable atmosphere (positive temperature gradient) in and below the canopy, and an unstable atmosphere above (negative temperature gradient). This is a prime example of the canopy intercepting the incoming shortwave radiation, leading to warming and instability at the canopy, while a stable atmosphere resides below the canopy height. In the profile, there are also slight variations in the average temperature near the tower platforms. These small, sharp, artifacts in the profile appear consistently for this weather type during the period of measurement, and may result from interaction between the sun and tower elements.

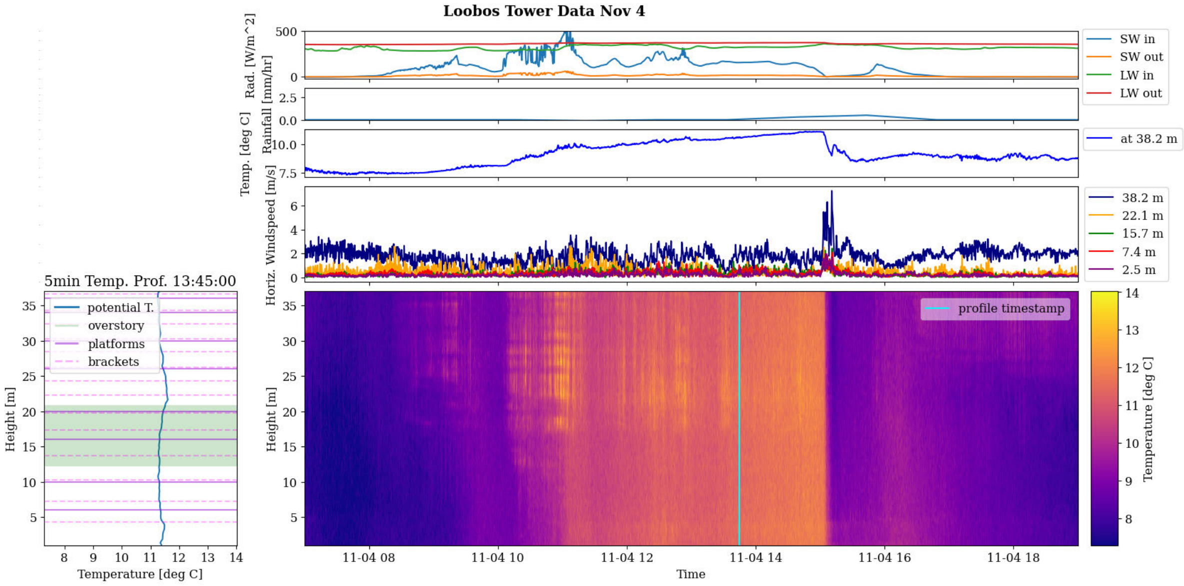

Figure 4.7: November 4th, 2022: a cloudy, windless day. The temperature profile (left) is marked on the temperature map (lower right). On the right side, from top to bottom: radiation, rainfall, temperature at a single height, horizontal wind speed, and temperature over height data for the duration of the measurement period.

Similar artifacts appear in the cloudy day profile, emerging as horizontal stripes in the late morning from 10:00-11:30 (Figure 4.7). This temperature map also displays a moment of rainfall just after 17:00, which aligns with a peak in wind speed. Moments with little to no cloud-cover align with the warmest temperatures. The profile during the early hours of the afternoon is slightly unstable above and below the overstory, which is stable to neutral. These regions of instability are likely due to heating of the canopy and forest floor. Excluding the time period of the rain shower, the low wind speeds and shear indicate that the wind would be less likely to contribute to the formation of turbulence. Therefore, turbulence during this cloudy day is likely driven primarily by surface heating.

Figure 4.8 depicts a windy day with very low values of incoming shortwave radiation, indicating thick cloud cover. Both the profile and the temperature map display a well-mixed atmosphere with almost no vertical variation in temperature under, throughout, and above the canopy. Slight decreases in cloud cover align with warmer patches in the temperature map. The air warms up slowly by a couple of degrees throughout the day, then starts to cool again towards the evening. Both of the windy figures (Figure 4.5 and Figure 4.8) appear grainy, like Figure 4.4, while covering similar temperature ranges (about 3.5 K). This texture could stem from this low temperature range, turbulence generated by wind shear, or a combination of both. Unlike the cloudy, windy night (Figure 4.5), there is no cold zone at the forest floor, while this day and night both have similar temperature ranges. The cloudy, windless, day also did not have the cold zone above the forest floor, adding consistency to the narrative that solar radiation heats the forest floor during the day. This also indicates that, even on cloudy days where the temperature profile appeared near neutral, the heat gathered at the forest floor was diffused through the understory air and/or conducted into the forest floor.

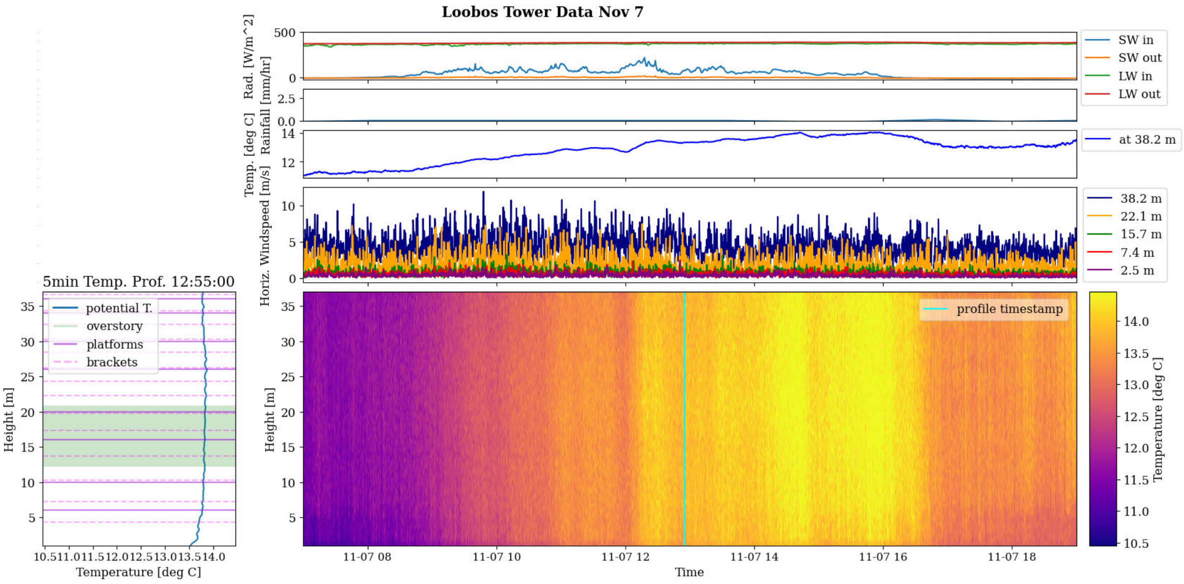

Figure 4.8: November 7th, 2022: a cloudy, windy day. The temperature profile (left) is marked on the temperature map (lower right). On the right side, from top to bottom: radiation, rainfall, temperature at a single height, horizontal wind speed, and temperature over height data for the duration of the measurement period.

4.2.3. Extra Features

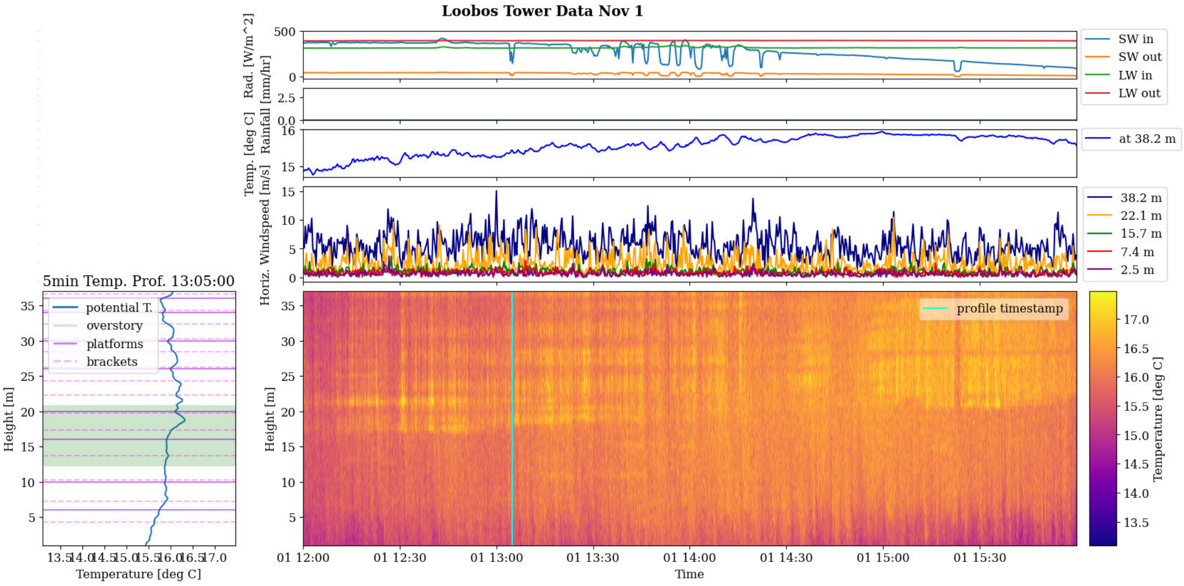

Figure 4.9: A few hours with mixed clear- and cloudy-sky moments on November 1st. The temperature profile (left) is marked on the temperature map (lower right). On the right side, from top to bottom: radiation, rainfall, temperature at a single height, horizontal wind speed, and temperature over height data for the duration of the measurement period.

Next to half days representing typical weather situations as explained in Section 3.4.2, rain, sun, and rapidly alternating temperatures were also studied. Many of the temperature maps display horizontal and vertical stripes, such as those displayed in Figure 4.9. The vertical stripes line up with the changes in cloud cover, and the horizontal lines often match the heights of the platforms and/or the brackets. Under sunny conditions, they could be caused by shading by the platforms, as this could lead to colder measurements than those taken in direct sunlight, despite the effects of the sun screen. Conversely, the sun reflecting off of or heating tower elements could also raise the temperature measured. Since these horizontal lines are likely due to the measurement set-up, they should not be taken as typical of the forest's atmosphere.

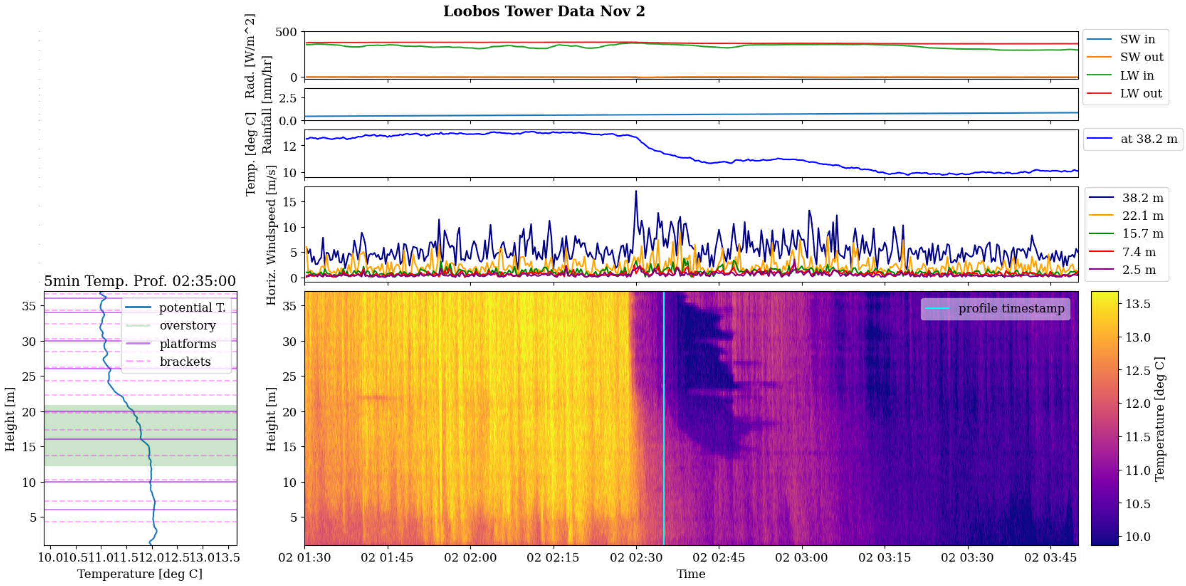

Figure 4.10: A few hours at night on November 3rd containing a rainstorm. The temperature profile (left) is marked on the temperature map (lower right). On the right side, from top to bottom: radiation, rainfall, temperature at a single height, horizontal wind speed, and temperature over height data for the duration of the measurement period.

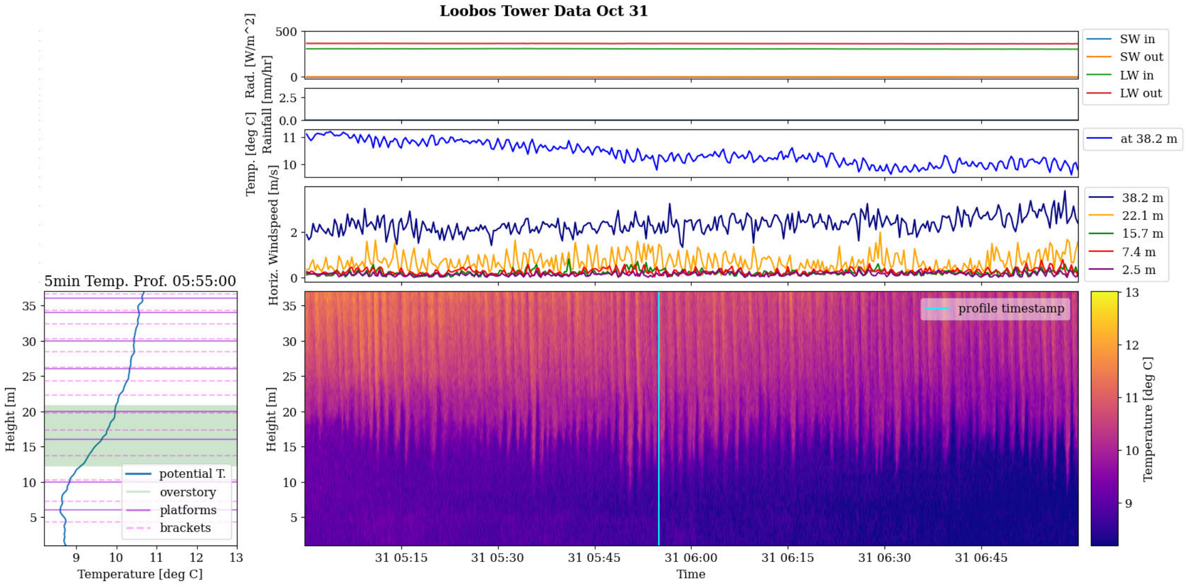

Figure 4.11: Slanted "fingers" of alternating warmer and colder air on the early morning of October 31st. The temperature profile (left) is marked on the temperature map (lower right). On the right side, from top to bottom: radiation, rainfall, temperature at a single height, horizontal wind speed, and temperature over height data for the duration of the measurement period.

Heavy rainstorms are easy to spot in the temperature maps, the air cools suddenly, and the brackets holding the fiber remain wet longer than the free fiber, leading to cold horizontal stripes at the bracket locations. The additional moisture provided by the rain is a source of latent heat flux. As water changes phase to gas, energy is consumed, thus lowing the temperature of the forest's surfaces as well as the air. In the case displayed in Figure 4.10, the wind well above and at the top of the canopy spiked at the beginning of the rain shower. The hourly measurements from the KNMI station at Deelen also reported a little rain around this time.

Another phenomenon, spotted on some clear, dry, nights with low wind speeds, were the "fingers", such as those displayed in Figure 4.11. On October 31st, this phenomenon featured a soft-sloped inversion with an average temperature difference of about 2 K between the air under and above the overstory. On a smaller time scale, the inversion is a bit sharper, and ranges between the canopy and about 10 m above the forest floor. These fingers slant at an angle of 0.61 m/s to 0.80 m/s from upper left to lower right, with a frequency of about 40 to 44 cycles per hour. This angle occurs above the canopy (below the canopy, the fingers are near-vertical). One possible explanation for this is that there are packets of cooler air moving vertically down from above into the canopy at a velocity of about 0.61-0.80 m/s and that this occurs 40-44 times per hour during this measurement period. Perhaps these packets then accelerate under the canopy so as to appear vertical, or colder air is transported in from the sides and/or mixed in from below. The frequency of this phenomenon matches that of the canopy waves (also referred to as gravity waves) described by Cava et al. (2004) and identified under similar meteorological conditions in Schilperoort et al. (2022). The bands differ in thickness and clarity, indicating that the time intervals during which the air at these locations is colder or warmer changes, and that the temperature contrast between warm and cold also varies. These differences in frequency and contrast are also reflected in the graph of the air temperature measured at 38.2 m height.

4.3. Inversion

4.3.1. All Days

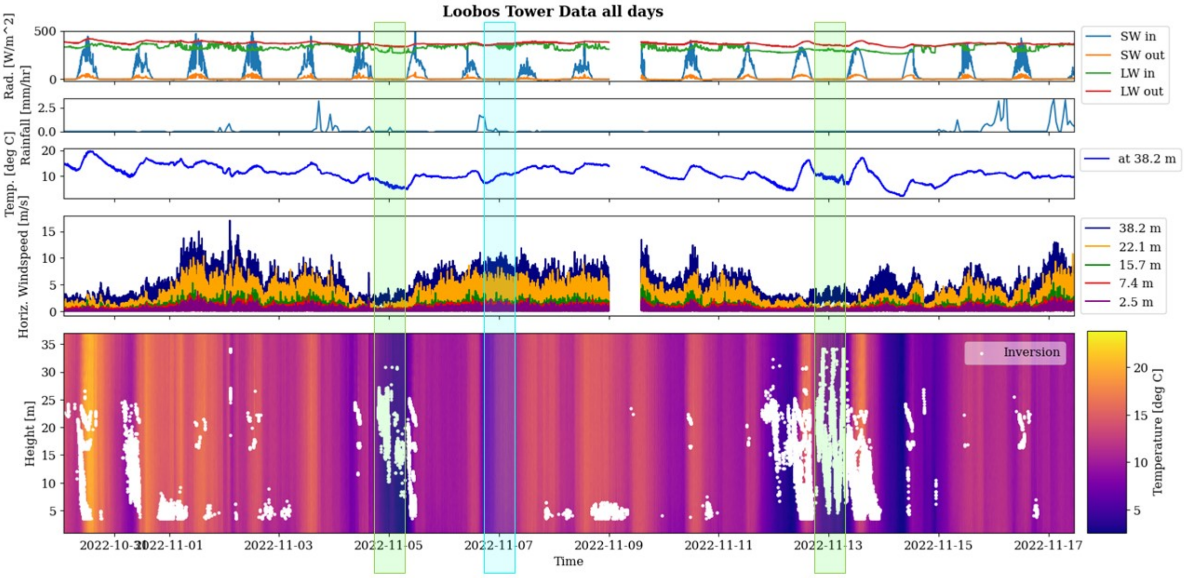

Figure 4.12: From top to bottom: radiation, rainfall, temperature at a single height, horizontal wind speed, and temperature over height data for the duration of the measurement period with calculated inversion heights. The boxes highlight the nights further analysed in this portion of the research.

The inversion heights calculated and filtered per the method described in Section 3.4.4 are displayed in Figure 4.12. Sometimes, the strongest temperature difference found resides in a zone close to the ground (such as on the nights of October 31st through November 1st, and from November 8th to 9th). This is likely due to the ground cooling the air close to the forest floor. The method used properly highlights strong inversion layers when they are present (such as on the night of November 4th and 12th). In the event of multiple inversions, the calculated inversion height sometimes jumps between them (nights of October 30th and November 12th). The hours with strong inversion layers reside in nights with low wind speeds. There are also some other points selected that correspond to none of these situations, and often align with tower platforms, fastening brackets, or a colder air pocket located at the canopy.

The two clear inversions on the 4th and the 12th are further analysed in this section. For comparison, the night of the 6th, which contained no inversions strong enough to pass the temperature screen, was similarly analysed as a control. Including these data indicates which findings may be due to the inversions, and which patterns may occur independent of a sharp temperature inversion. The variables included in this analysis are inversion heights and strengths, along with various meteorological data (longwave radiation, wind speed, and wind direction). Wind direction and longwave radiation presented no correlation to the inversion on all three nights, and are included in the Appendix rather than the main text.

Table 4.1: Coefficients of determination (r^2) for a best line of fit between various meteorological variables for calculated inversion heights from October 30th 02:00 through November 17th 11:00.

	r^2 for all days [-]			
Wind speed at measurement height [m]	Inversion height	22.1 m wind speed	15.7 m wind speed	7.4 m wind speed
38.2	0.07	0.23	0.25	0.23
22.1	0.17	1	0.34	0.16
15.7	0.23	0.34	1	0.34
7.4	0.06	0.16	0.34	1

Table 4.1 summarizes some of the coefficients of determination for all the data screened using the method described in Section 3.4.4. More detail can be seen in Figure A.2, which displays inversion height versus wind speed at the four measurement heights, and in Figure A.3, which shows how the wind speed of one height correlated to another. Out of the inversion height-to-wind speed comparisons, the wind speed measured at 15.7 m relates the most to the inversion height, with an r^2 of 0.23, followed by the wind speed measured at 22.1 m. The low coefficient of determination occurs since this comparison contains all the calculated inversion data points, grouping the data of the various inversions together, as well as taking the points located by the calculation that do not actually represent inversions into account. The 15.7 m wind speed is also more closely linked to the neighboring wind speeds than the 38.2 m wind speed. This indicates that, on average during the periods of measurement with strong enough temperature inversion to be factored in, the wind throughout and under the canopy was better coupled than the wind well above the canopy. The overstory likely blocked the above-canopy wind, causing turbulence, mixing, and less uniformity between the wind measured above and below the canopy. These low coefficients of determination also serve as an indication that wind speeds at the heights between measurements can vary significantly; the measurement at 15.7 m is not necessarily representative of the wind speed at a 19 m height. This implies that the changes in the wind speed at these discrete heights is not fully representative of the changes in wind speed at the inversion heights.

4.3.2. November 4th, 2022

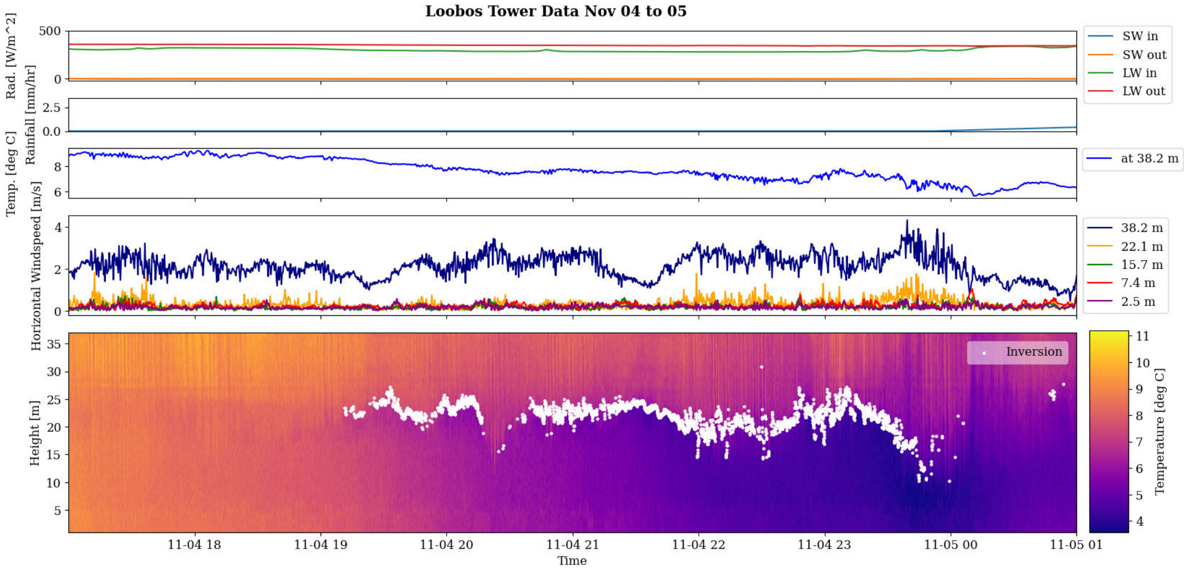

Figure 4.13: Calculated inversion heights for November 4th, together with meteorological data (from top to bottom: radiation, rainfall, temperature at a single height, horizontal wind speed, and temperature over height).

The inversion of November 4th dissipated when the wind speed increased and clouds formed around midnight. Peaks in wind speed appear to align with drops in inversion height, along with an increase in the spread of the calculated inversion heights (the white dots appear noisier). The calculated inversion heights, displayed in Figure 4.13, mostly reside between 15 m and 25 m. In general, this night was cool, clear, and maintained low wind speeds.

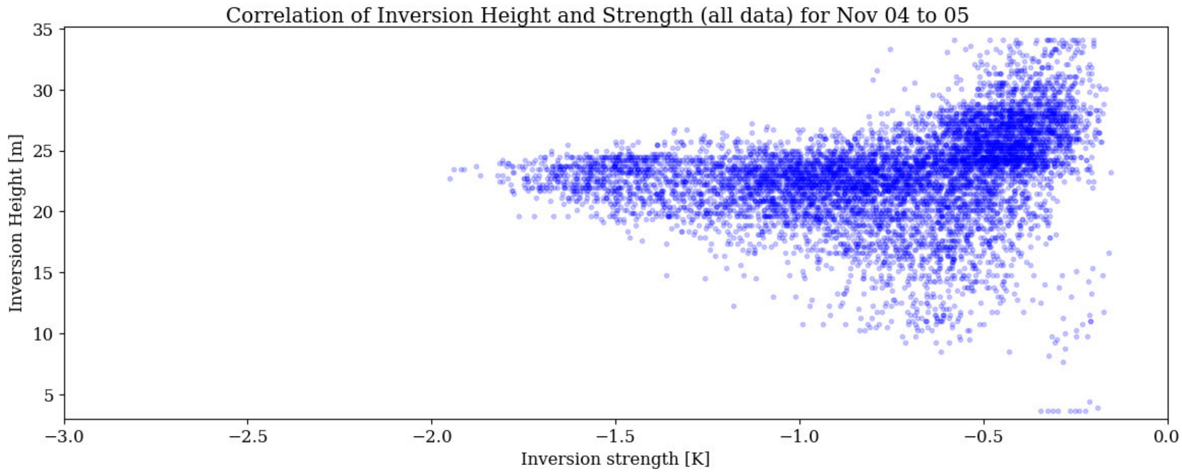

Figure 4.14: Inversion strength versus height on the clear, cool, near-windless night of November 4th, data not screened based on inversion strength.

In Figure 4.13, the inversion appears to strengthen the most when it resides just above the canopy. This is supported by Figure 4.14, in which there appears to be a nonlinear relationship between the inversion height and the inversion strength. On the 4th, the strongest inversions occurred in the zone a few meters above the canopy, with weaker inversions throughout the overstory and above the canopy, and the weakest inversions further above the canopy height.

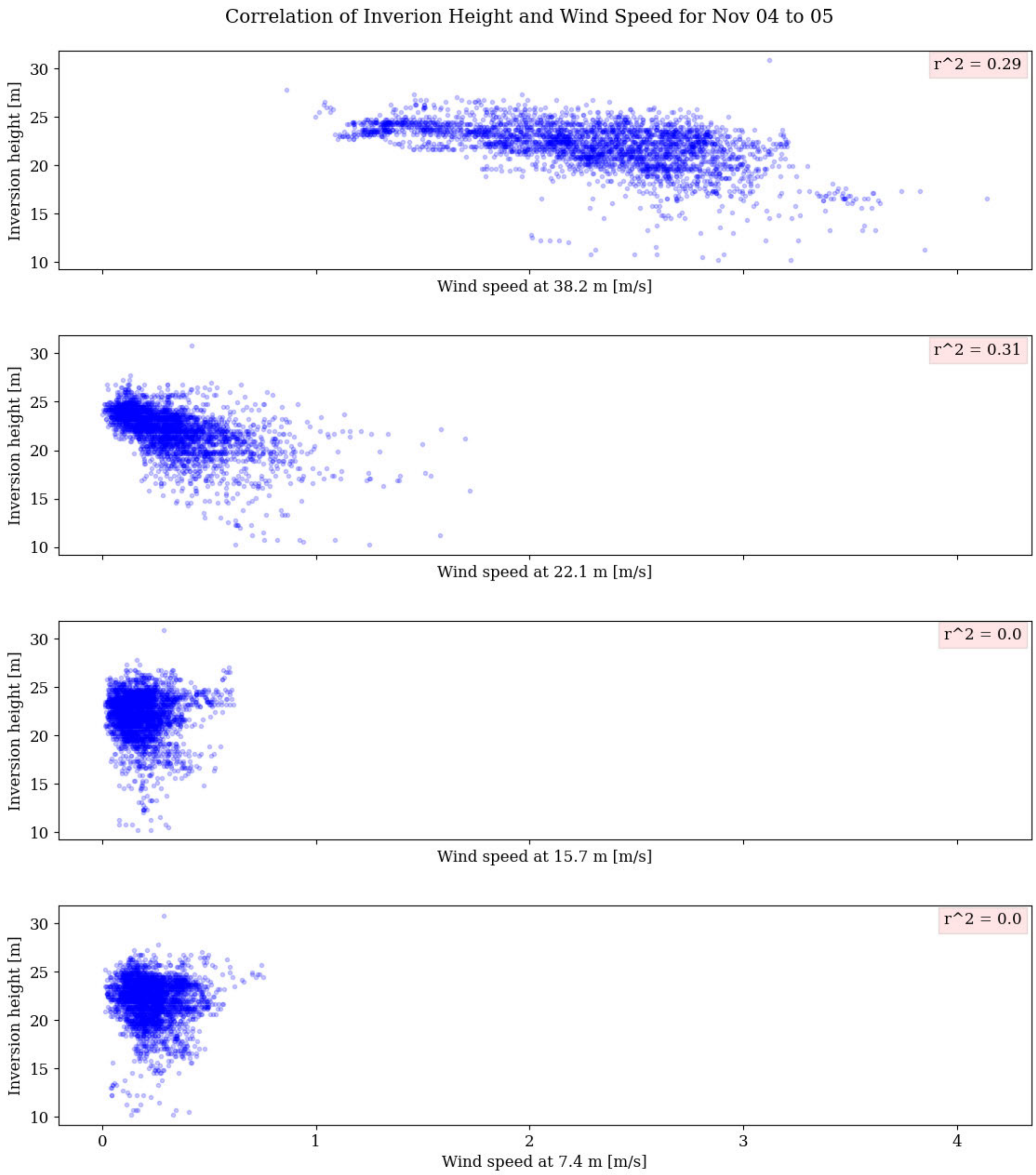

Figure 4.15: Wind speed versus inversion height on the clear, cool, near-windless night of November 4th. Correlation coefficients (r^2) for a best line of fit are displayed in the upper right corners.

The plots displaying wind speed versus inversion height (Figure 4.15) support the observation from Figure 4.13 that wind speed correlates negatively with the inversion height. The inversion height drops as both the 22.1 m and the 38.2 m wind speeds rise. The 15.7 m and the 7.4 m wind speeds display no visible correlation with the inversion height, and the correlation coefficient under a linear best line of fit is zero, indicating that wind speeds at these heights are either too low to measure accurately or not linked to inversion on the 4th. To gain insight into which of these is more likely, the wind speed data can be analysed.

The relatively strong correlation and coefficient of determination between the 7.4 m and the 15.7 m wind speeds displayed in Figure 4.16 indicates that the low wind speeds at these heights are valid measurements rather than signal noise (these graphs contain the non-interpolated wind speed data, which do not display much difference to similar graphs implementing the interpolated data used for inversion identification, displayed in the Appendix). This, combined with the lack of correlation between the 15.7 m and 22.1 m wind speeds shows that decoupling somewhere between these heights is likely. One possible explanation for the low correlation and coefficient of determination between the 38.2 m and the 22.1 m wind speeds is that these may be coupled during sections of the time period measured, and decoupled during others (such as when the inversion height rises to between these measurement heights). The coefficient of determination is likely slightly misrepresentative as wind speed profiles are typically logarithmic in the lower portion of the ABL (Abubaker et al., 2018), which would lead to a curved scatterplot. Despite this, it can be used as a metric to give a rough indication as to whether or not the wind is coupled since these heights are close to each other.

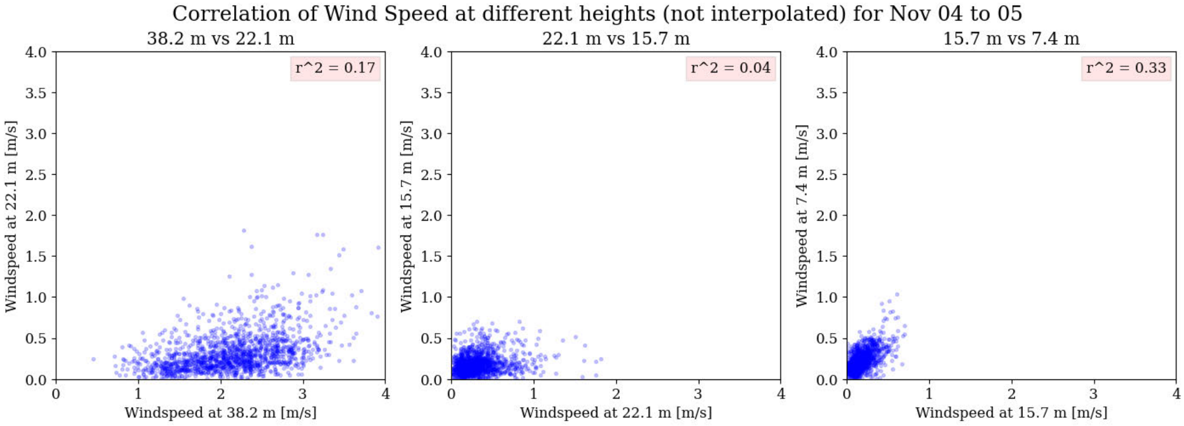

Figure 4.16: Wind speed versus wind speed from non-interpolated meteorology data at various heights on the clear, cool, near-windless night of November 4th 17:00 to November 5th 01:00. Correlation coefficients (r^2) for a best line of fit are displayed in the upper right corners.

The variability of the wind speed (visible in the magnitude of the short-term variation in the wind speed plot in Figure 4.13) increased and decreased together with the wind speed, and, by extension, with the inversion height. The inversion height and the standard deviation of the wind speed on the night of November 4th, displayed in Figure 4.17, correlate well for the 22.1 m wind speed, which is supported by an r^2 of 0.30 (as compared to an r^2 of 0.10 for the other heights). The 22.1 m wind speed and inversion height linking more closely during this time period than the other wind speeds makes sense, as the inversion height is mostly around the canopy for these data, so this is the closest measurement height.

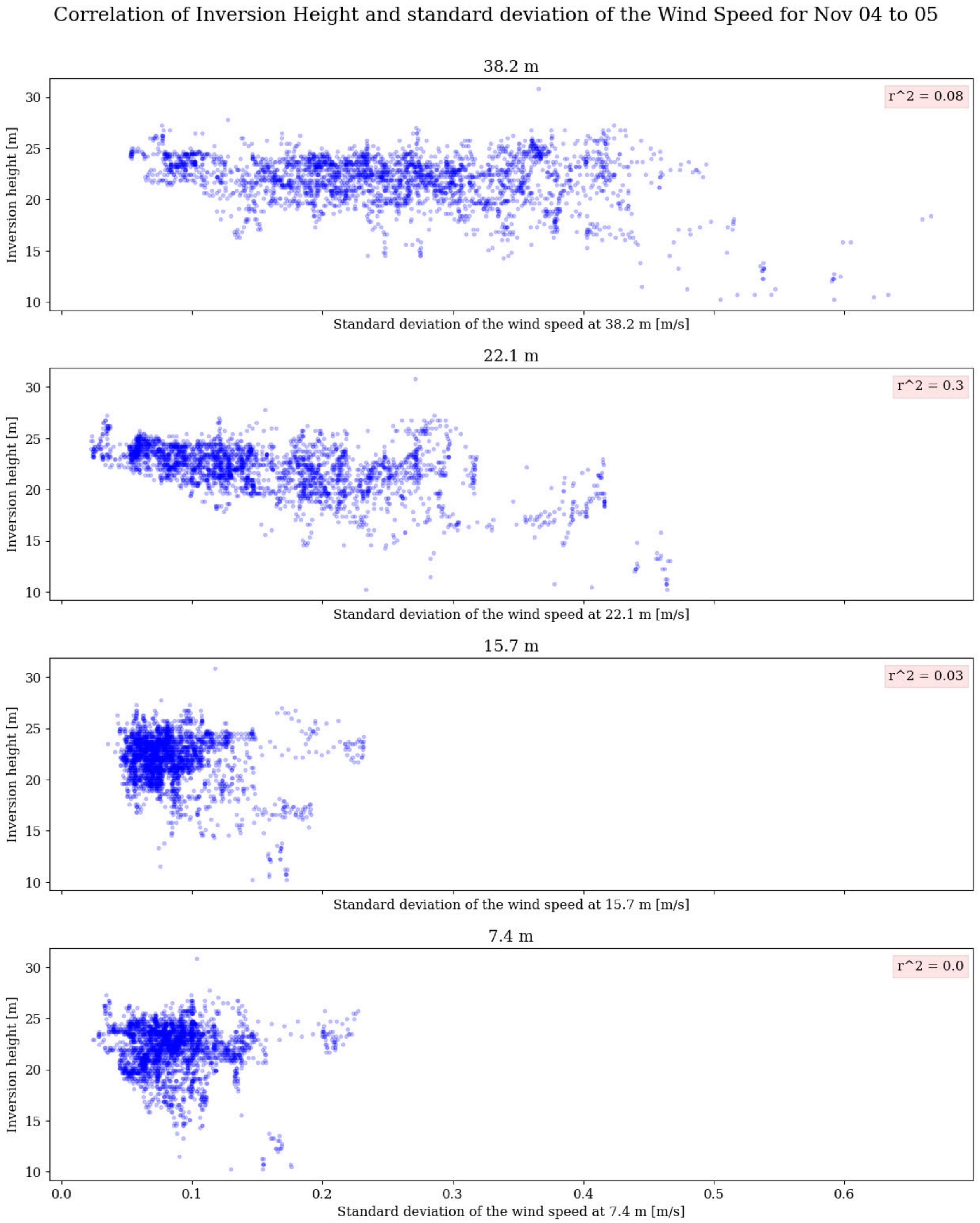

Figure 4.17: Standard deviation in wind speed versus inversion height on the clear, cool, near-windless night of November 4th.

4.3.3. November 12th, 2022

The inversion heights on the night of November 12th (displayed in Figure 4.18), are well defined and fluctuate between a few meters above the forest floor to a few meters above the canopy. From 21:10 - 21:40, the calculation for inversion height picks up a second inversion located at 30 m, rather than the one closer to the canopy. As on November 4th, the wind speed appears to vary together with the inversion height, the inversion height climbs to a few meters above the canopy when the wind is calmer, and drops increasingly as the wind speed mounts and varies. On the 12th, however, the range of heights between which inversion oscillates is much larger than the previous example.

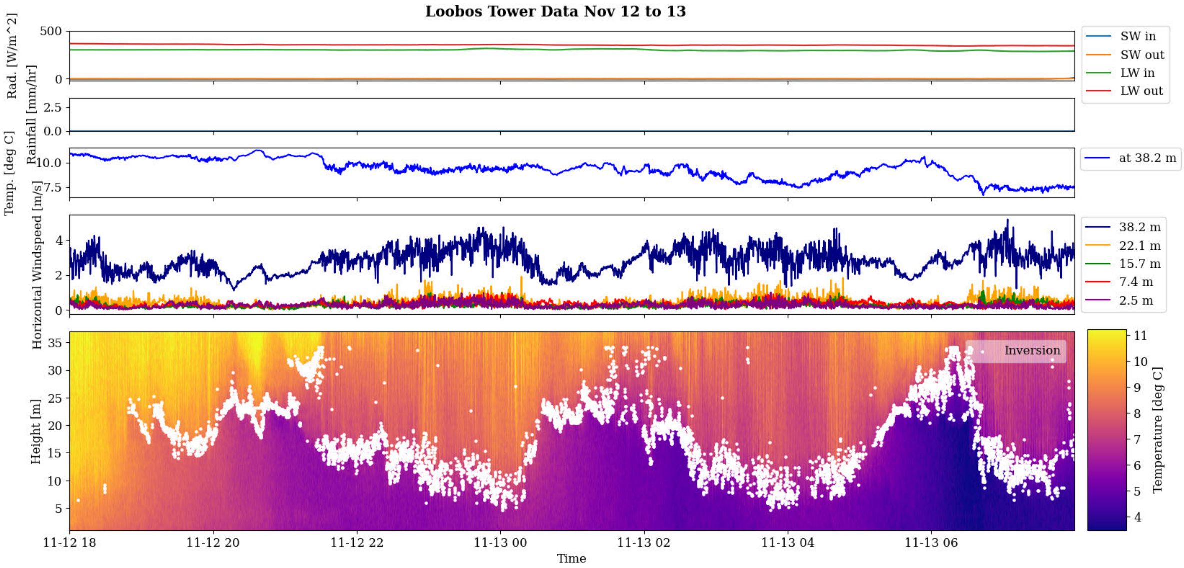

Figure 4.18: Calculated inversion heights for November 12th, together with meteorological data (from top to bottom: radiation, rainfall, temperature at a single height, horizontal wind speed, and temperature over height).

The night of November 12th showed no clear correlation between inversion strength and height (see Figure 4.19). The strongest inversions occurred most frequently a few meters above the canopy. Some strong inversions also materialized between 8 m and a few meters into the base of the foliage layer. Between these heights, a gap in very strong inversion measurements exists, indicating that the strongest inversions did not take place in the foliage layer.

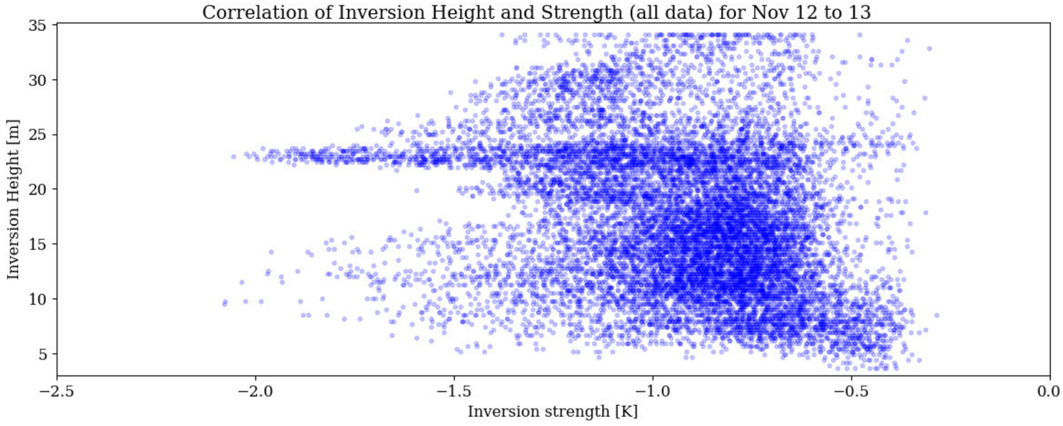

Figure 4.19: Inversion strength versus inversion height on November 12th to 13th, a cool, clear night displaying a strong, sharp, temperature inversion and low wind speeds.

The wind speeds at 38.2 m, 22.1 m, and 15.7 m all correlated to the inversion height (Figure 4.20). As on November 4th, the lower wind speeds fell together with greater inversion heights. In the figure, there appears to be a curve to the scatter distribution, with the inversion height dropping off relatively quickly a the wind speed increases. This indicates that the inversion height rose above the canopy only under very wind still conditions. It could be that the slight wind shear generated at higher wind speeds near the canopy caused mixing, thus breaking through the inversion, mixing the cooler air below with the warmer air above, and driving the inversion closer to the forest floor.

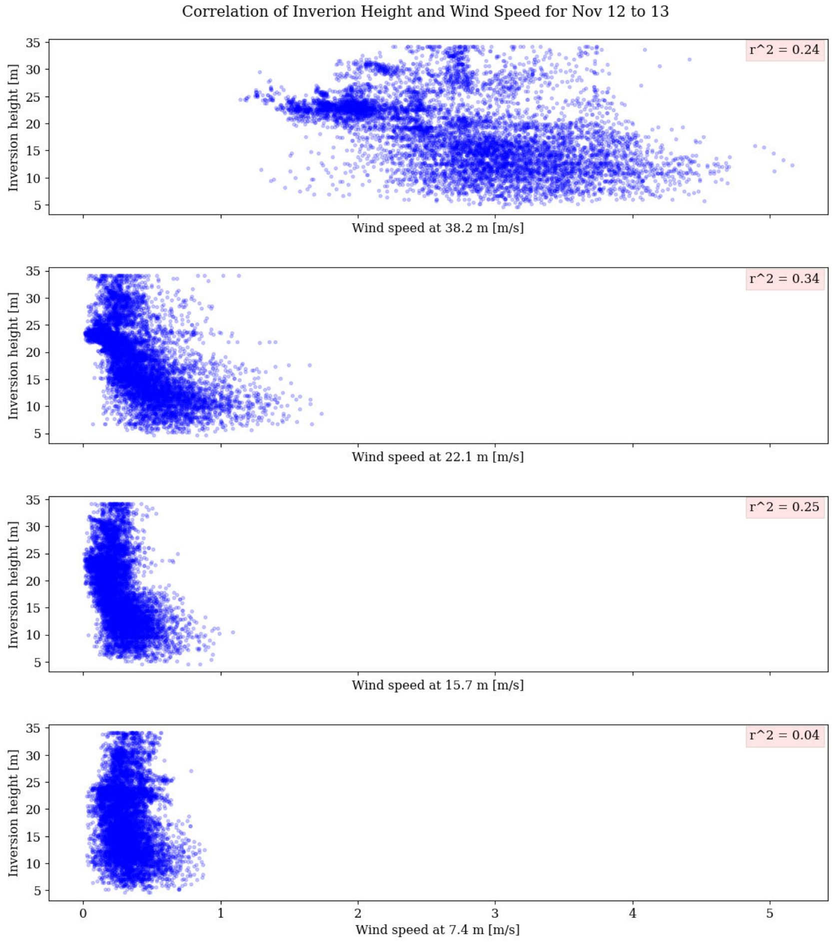

Figure 4.20: Wind speed measured at various heights versus inversion height on November 12th to 13th, a cool, clear night displaying a strong, sharp, temperature inversion and low wind speeds.

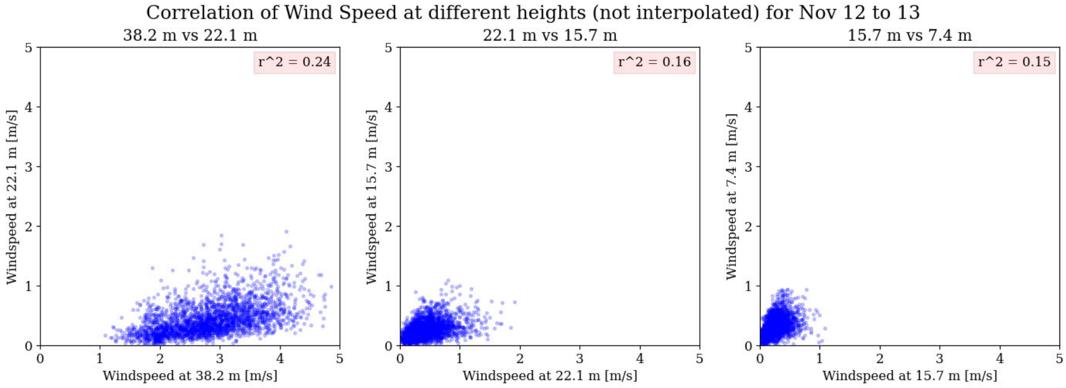

Figure 4.21: Wind speed versus wind speed from non-interpolated meteorology data at various heights on November 12th to 13th, a cool, clear night displaying a strong, sharp, temperature inversion and low wind speeds. Correlation coefficients (r^2) for a best line of fit are displayed in the upper right corners.

On November 12th, the 38.2 m wind speed was better coupled tp the 22.1 m wind speed (supported by Figures 4.16 and 4.21). The 12th shows significantly more coupling throughout the overstory (between the 15.7 m and 22.1 m wind speeds), and less between the 15.7 m and 7.4 m wind speeds.

The inversion height correlates strongly to the standard deviation in the wind speed in Figure 4.22. Much of the change in inversion height over time can be explained by a linear model to the standard deviation of the wind speed (as demonstrated by the r^2 values). The same curved trend displayed in the scatterplots in Figure 4.20 occurs, perhaps even more clearly, in Figure 4.22, where middling inversion heights correspond to relatively low standard deviations. Due to the curve in the data, these coefficients of determination would be even higher for a curved line of fit.

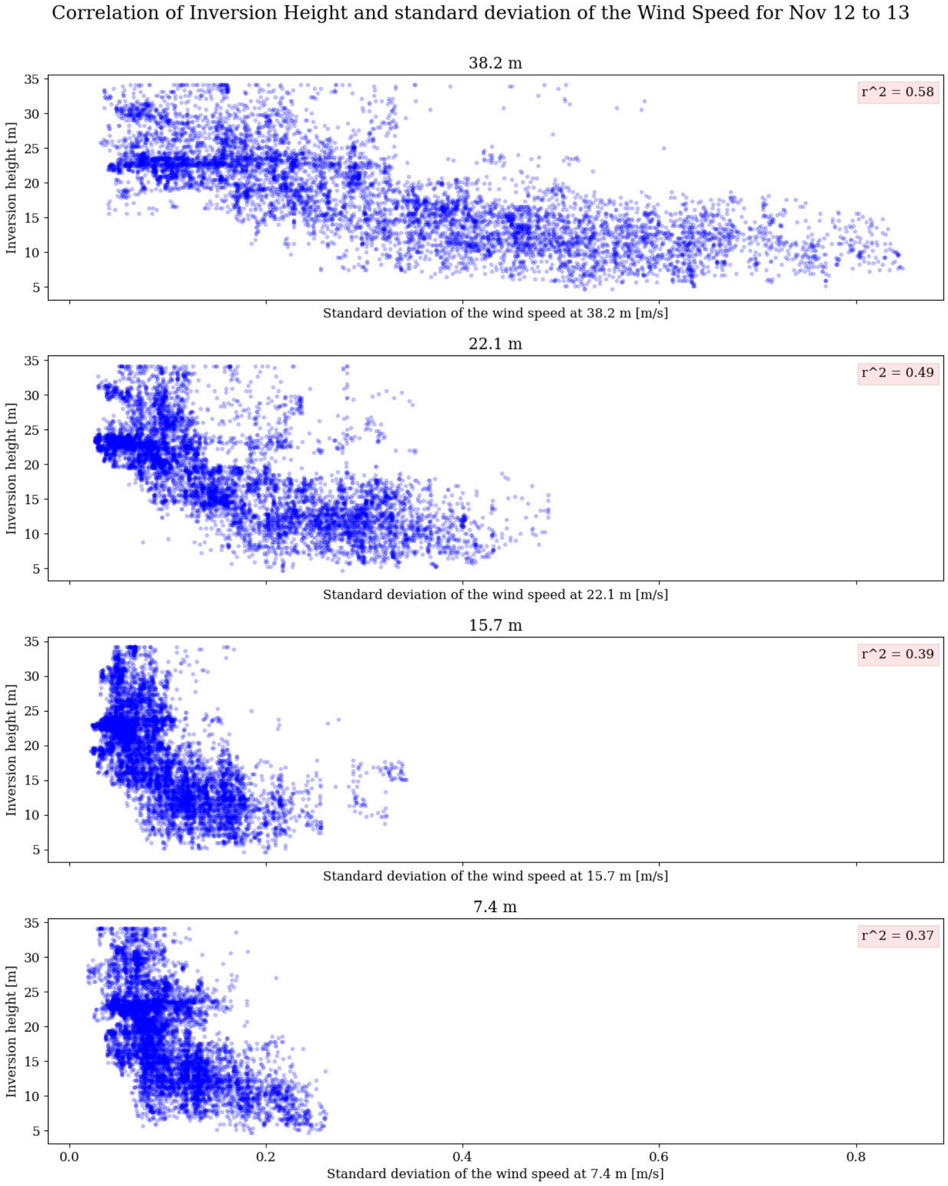

Figure 4.22: Standard deviation of wind speed versus inversion height on November 12th to 13th, a cool, clear night displaying a strong, sharp, temperature inversion and low wind speeds. Correlation coefficients (r^2) for a best line of fit are displayed in the upper right corners.

4.3.4. November 6th, 2022

On November 6th, a cloudy, windy, night with little rain, there was no inversion layer detected. The points of greatest temperature difference as calculated by the method described in Section 3.4.4 appear noisy, with a greater density of points grouped closer to the ground (see Figure 4.23). None of the points had a great enough temperature difference above and below to pass through the temperature screen. On this night, there was no correlation between these points and the wind speed, as indicated in Figure A.15. No relationships were found between wind speed or other meteorological factors and calculated inversion height on this inversionless night. For comparison, the correlations of the unscreened data for the nights with inversion were examined. While weakened by including many non-inversion data points by not screening based on temperature difference, the nights with inversion still displayed correlations between wind speed and inversion height when processed in the same manner as the data from November 6th (see Table A.1 for the coefficients of determination as a qualitative method of comparison).

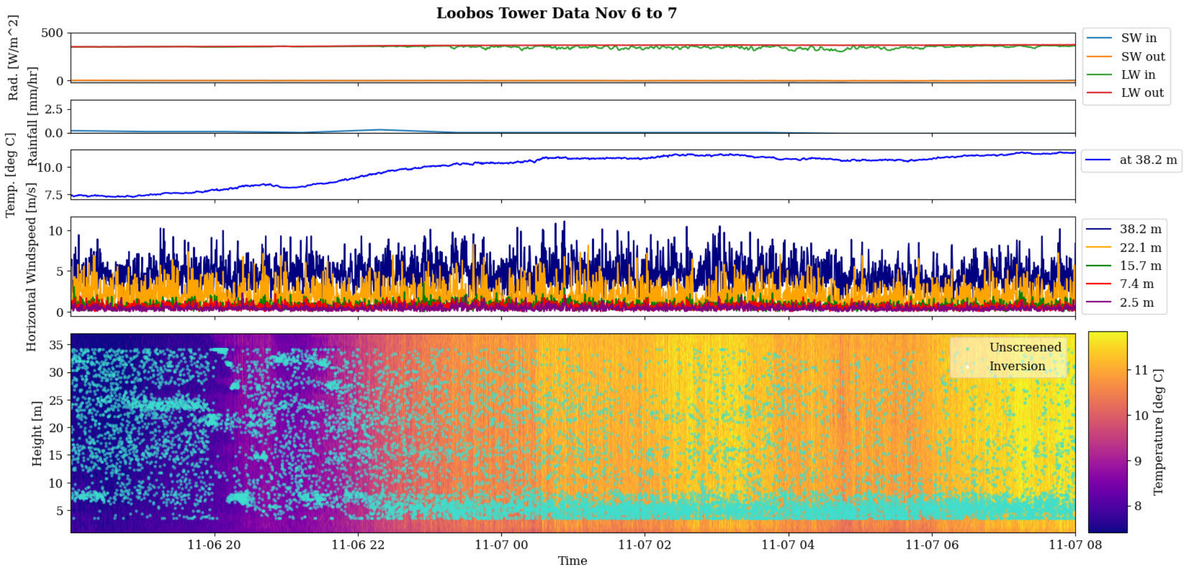

Figure 4.23: All calculated inversion heights, including those without screening based on temperature difference (labeled as "Unscreened"), for the windy, cloudy night of November 6th, together with meteorological data (from top to bottom: radiation, rainfall, temperature at a single height, horizontal wind speed, and temperature over height).

5

Discussion

The DTS running at Loobos recorded temperature profiles over the course of a few weeks, capturing temperature gradient data for a range of meteorological conditions and revealing a few nighttime inversion layers. Creating temperature maps (temperature profiles over time) provided an overview of general patterns in vertical temperature distribution, and linking the DTS data to other meteorological data placed the profiles and maps into context. The individual profiles allowed for a closer look into the development of the various phenomena shown in the temperature maps.

Temperature constitutes a component of the weather. Other components of the weather showed clear links to the vertical and temporal distributions of temperature at the measurement site. Both the profiles and the temperature maps provided insight into how heat moves and where it resides below, throughout, and above the canopy. The one second profiles provided detailed information on each time step; comparing back-to-back profiles indicated how the structure of the air changed from one moment to the next. While unclear with the current set-up and processing, these one second profiles may hold the potential to display individual eddies of warm or cold air, and are discussed further in Section 5.1. Averaged profiles over small time intervals (on the scale of seconds to minutes) yielded more robust insights into the structure of the air in the forest at a given moment. Profiles averaged over longer time intervals (tens of minutes to hours) provided more general insight into what the temperature structure was like on a given day. Temperature maps (examined further in Section 5.2), while containing less detailed information of each individual measurement, provided more information into trends and patterns throughout a time period than the temperature profiles. For example, revealing diurnal warming and cooling, as well as trends in inversion layer height (Section 5.3). Combining profiles with maps helped interpret the DTS data; the profiles indicated both stability and where the influence of tower and overstory features might have played a role, while the maps showed how the distribution of temperatures shifted over time and which times might be interesting to study further. Coupling the temperature maps and profiles with meteorological measurements provided further context and helped validate and clarify the results.

5.1. Individual Eddy Tracking

Likely eddies could be identified in the data, but these would need further verification using another method for validation. Tracking these eddies or determining eddy properties, such as size and speed, was not possible with the method implemented. The profiles generated by the DTS revealed many temperature fluctuations. Comparing the individual profiles to the rolling average data, as displayed in Figure 4.1, showed that some of the fluctuations may arise from measurement noise, while others are highly likely to be significant signals due to local eddies. When comparing the signals well outside of the noise level in these profiles over time, it was not possible to determine whether signals at two different time steps corresponded to the same eddy. A set of profiles generated over sequential time steps can be seen as a stop-motion view of the air over time. In this way, a warm eddy captured in sequential frames would be expected to manifest as a positive-temperature signal traveling up the fiber. However, the frames in between two strong positive signals, that might indicate a traveling eddy, often showed weaker positive signals, making it hard to differentiate between these signals and noise. Removing these frames due to uncertainty caused by noise reduces the likelihood that the two positive signals belonged to the same eddy.

The set-up, method, and processing tested in this study may have led or contributed to an inconclusive result. Some set-up and method-related options that could improve certainty include: using a more sensitive fiber with a higher response time; running a device such as the Silixa Ultima S (allows for double the spatial resolution of the Ultima M, but even the Ultima S tends to under-measure high frequency temperature fluctuations (Peltola et al., 2021)); building a 2D or 3D grid to account for horizontal transportation, and removing the sun screens. Running the fiber up and down along a vertical plane, interpolating between the generated temperature profiles to create a 2D grid of temperature data, and then viewing these data slices over time, could potentially yield results that a single-fiber method does not. The study by Thomas et al. (2012) implemented the DTS in a 2D setup over a field and was able to determine vertical eddy scales, perhaps a similar method of processing could work in a forest. A 3D set-up could also be tested, with fibers strung vertically up and down along multiple vertical planes set next to each other (essentially creating a cube-like shape in which data are gathered). As eddies are 3D structures (Kleissl & Garai, 2011), observing them in more dimensions than the 1D set-up used in this study could provide extra insight. The sun screens, while yielding a more accurate reading of the temperature, affect the air flow around the fiber, and thus could have influenced the effectiveness of this method of eddy tracking.

It could also be that these data do allow for individual eddy tracking under a different method of data processing. Perhaps combining points to decrease uncertainty due to noise (changing the resolution from every quarter meter to a half a meter) would create clearer signals for large enough eddies and decrease the signal noise. Another option would be to perform the same analysis on the data gathered from the other side of the fiber (the one encased in cotton, to be used for wet bulb temperature) and line up the signals based on height above the ground. Averaging these signals would be another way to decrease uncertainty, since there would be more data points per meter. Implementing a wavelet analysis method (which allows for analysis of the various signals based on their scale) would structure this cumbersome process, increasing accuracy and allowing for mass processing of the data (Torrence & Compo, 1998). Recently, wavelet analysis has been implemented in various atmospheric studies to identify eddies, such as Curto & Gassmann (2022)'s research concerning isolating coherent structures over crops.

Another possible reason why individual eddies could not be tracked in these data is that the temperature differences between the eddies and the average air temperature were not large enough to be picked up on during the given days. Peltola et al. (2021) measured temperature perturbations up to 1.5 K during a day in June, and up to 1.0 K at night throughout a 17 m tall pine forest with sonic anemometers. The DTS on-site there reported similar ranges. These ranges are larger than those seen in much of the Loobos data, which may be due to the slightly warmer temperatures, season, time of year, and/or the data selected by Peltola et al. (2021) to display. The days studied in the Loobos data were limited to the few with low wind speeds. It could be interesting to look into what this method of data processing and gathering would lead to on a day with lots of heating due to incoming solar radiation, such as might occur in late spring. Testing and refining this method over a different surface type, such as a field, rather than measuring through the forest canopy, might also help clarify the signal and indicate whether this method holds potential.

Next to the limited range of weather types measured, there are other potential sources of error for all measurements discussed in this study. The measurements were made at only one location, so the patterns and trends described may not be typical for this forest, let alone forests in general. Furthermore, the data only represent two and a half weeks, rather than trends that occur consistently over a longer period of time. The fiber also resides closer to the tower than the trees, meaning that the data represents potential effects due to both the small clearing surrounding the tower and the tower itself.

5.2. Distribution of Temperature

The vertical and temporal distribution of temperature at the measurement site clearly linked to various components of the weather. Both the profiles and the temperature maps provided insight into how heat moves and where it resides below, throughout, and above the canopy for the duration of the experiment. Coupling the DTS data with meteorological measurements provided further context and helped evaluate and clarify the results. Phenomena recognized in the DTS data included rain showers, sunlight versus cloud cover, (changes in the) vertical distribution of air temperature (such as canopy effects), "fingers", and inversion layer height and strength.

Both direct sunlight and rainfall led to changes (often sharp) in the measured vertical and temporal temperature distributions. Rain storms suddenly dropped the temperature (inducing change along the temporal axis), and could also lead to vertical differences in the measured temperature, such as the horizontal stripes seen in Figure 4.10. These vertical differences occur when evaporative cooling lowers the temperature of wet sections of the fiber. Therefore, rain can result in an inaccurate air temperature measurement, but may provide insight into the temperature of other wet forest surfaces exposed to similar wind speeds, such as nearby tree trunks. Daytime changes in cloud cover on a scale of minutes to hours consistently led to warmer zones in the temperature measured with the DTS at moments with more sunlight, and colder zones during those with more cloud cover. The effects of direct sunlight on the vertical temperature distribution were twofold. The first effect, a general increase in the temperature measured above the canopy, matches the expectations of the literature (Moene & Dam, 2014). The second effect, sharp jumps over a small vertical scale (like those in Figure 4.9) lined up with tower features, and likely occurred due to measurement error. Measurement error due to direct radiation likely caused these sharp contrasts, they occurred on both windy as well as windstill days, meaning that increased mixing of the air had no effect on the sharpness of the artifacts in the temperature profiles measured. Therefore, these horizontal lines are likely the effect of direct sunlight passing through the screen. This potential error further supported by Schilperoort et al. (2018), where, while the use of screens significantly reduced error due to solar radiation, a deviation of up to 1 K persisted.

The temperature maps displayed changes in the vertical distribution of air temperature at the measurement location, indicating the atmospheric structure under, through, and above the canopy. On very windy days, the aforementioned sun and rain effects were some of the only prominent patterns visible in the vertical temperature profiles as the air was well-mixed. The other noticeable features were a cooler zone in the first few meters above the forest floor at night and, occasionally, a cooler zone at the canopy. The cool zone near the forest floor is likely caused by a contrast between the ground and air temperature, along with low near-ground wind speeds. Clear days with low winds provided more variation and structure than their cloudy, windy counterparts.

The typical vertical temperature distribution for forests mentioned in Moene & Dam (2014) appeared under certain weather conditions. During clear days with low wind speeds, the warmest zone, while very weak, was often near the canopy, and, unless there was a strong inversion present, the canopy cooled off slightly more than the surrounding air at night. Even on windy or cloudy evenings, the cool canopy zone could still sometimes be spotted (see Figure 4.5). According to Moene & Dam (2014) and Foken (2021), the interception of incoming shortwave radiation and subsequent heating at the canopy generates the most turbulence, and there is less turbulence under the canopy than above during the day. In the data gathered at Loobos, the stronger turbulence should manifest as stronger variations from the mean temperature in figures like Figure 4.1. However, examining these profiles during time periods with a warm zone right above the canopy failed to yield clear patterns. The measured canopy effects might have been weakened in Loobos due to the sparse canopy, as well as the clearing around the tower. The fiber placement means that the fiber measured a zone with a break in canopy, as well as picked up any potential tower effects on air temperature and heat transfer. To properly assess this and the extent of these effects, measurements would need to be taken through the trees nearby. Ideally, both locations would gather data year-round, as the ability of a forest to act as a heat sink shifts, not just diurnally, but also seasonally (Oliphant et al., 2004). In these data, it appears as though higher wind speeds partially negate the effects of a canopy, decreasing the magnitude of vertical differences in temperature. Generally, the moments with higher wind speed also display more wind shear, which is a key driver of turbulence (Moene & Dam, 2014). Therefore, the general trend present of decreasing vertical temperature variation with increases in wind speed can be explained by the resulting increase in mixing due to wind shear.

The "fingers" displayed in Figure 4.11, appeared in the data on 30th and 31st of October, as well as on the nights with inversion. The only conditions under which clear fingers formed, likely canopy waves, were low-wind, clear nights with low inversion heights. When the inversion layer rose to above the canopy, the fingers weakened or disappeared all together. According to Cava et al. (2004), canopy waves may form due to Kelvin-Helmholtz instabilities at the canopy, which are triggered by wind shear. These likely only occur on the low wind speed days because at high wind speeds, the horizontal movement of the air overrules the vertical rising and falling of air that generates the band-like appearance visible in Figure 4.11. As a result, the air mixes more evenly and this phenomenon disappears. Under windstill conditions, not enough shear is generated to cause the Kelvin-Helmholtz structures, thus no bands can form. It would be interesting to know if this pattern occurs in other locations and if the angle of the fingers is consistent over time and space, as well as what causes the angle. Schilperoort et al. (2022) found similar artifacts, and deduced that they stemmed from either cold air dropping from the canopy, advection from the sides, or radiative cooling. The angle found in the fingers in Loobos would indicate that either the third option, or a fourth mechanism (wind above the canopy mixing plumes of warm air with the cooler air in and above the overstory), are other possibilities.

5.3. Inversion

Inversions formed during clear nights with low wind speeds. The heights of these inversions correlated strongly to certain wind speed characteristics. However, these inversions did not correlate well to the wind direction, nor to the longwave radiation (neither to the incoming or outgoing longwave radiation, nor the difference between the two). Schilperoort et al. (2022) also located wavelike inversions in a forest, and found no correlation between net radiation measured in the understory (rather than above the canopy, as was done in this study) and inversion. They did find a pattern between the wind speed at a 1 m height and the inversion height similar to the one described in this study, but did not see such a pattern in the above-canopy wind speed measured at 48 m. At the Loobos site, no correlations were discovered between inversion strength and the meteorological data tested. Inversion height and strength also showed little overall correlation, though the strongest inversions occurred most frequently a few meters above the canopy.

The nights of the 4th and the 12th of November, while both showing clear inversions, did not display all the same patterns. One big difference in the circumstances under which inversion took place occurred in the wind speed profiles. While the wind above and below the canopy was coupled on the 12th (see Figure 4.21), the 4th showed a distinct decoupling (see Figure 4.16) between the 22.1 m and the 15.7 m wind speed. This decoupling, linked with the inversion height mainly sitting around the top of the canopy on the 4th, explains why the inversion height on that night correlated to characteristics of the 22.1 m (and a bit to the 38.2 m) wind speed, and not so much the other wind speed measurements. In contrast, the inversion height on the 12th ranged from a few meters above the forest floor to well above the canopy, and displayed correlations to all four wind speeds. During its strongest moments, the inversion strength on the 12th was also slightly greater than on the 4th. The 12th also showed higher correlations between wind speed and variability and inversion than on the 4th. According to Schilperoort et al. (2022), inversion can form as a result of decoupling. Based on these data, both the height and strength of decoupling may play important roles in determining the range of inversion heights.

The reason for the differences in these inversion characteristics could lie in the differing circumstances preceding inversion. The day of the 4th displayed intermittent sunlight in the morning, developing into an overcast afternoon, with a rain shower at 15:00, little to no wind under and through the overstory, a bit of wind (about 4 m/s) above the canopy, and temperatures between 7-14 °C (about 3 degrees colder than the day before). The day of the 12th was dry and almost cloudless, with almost no wind (1-3 m/s above the canopy, less than 1 m/s below), and temperatures between 4-20 °C (about 7 degrees warmer than the day before). The larger gradient between ground and above-canopy temperature may have led to stronger inversion on November 12th, and the lack of decoupling may tie into why the inversion height moved more (though it could also be that the 4th experienced more decoupling precisely because the inversion remained relatively steady).

Both nights displayed a relatively strong correlation between the wind speed and inversion height, as well as between the standard deviation of the wind speed and the inversion height. These trends are reflected in the coefficients of determination, which, while less appropriate than a better fitted model due to the assumption of a linear correlation, still present an indicator for how closely two variables link together. On the 4th, the strongest coefficients of determination with respect to inversion height were with the 22.1 m wind speed (r^2=0.31) and standard deviation of the wind speed (r^2=0.30). On the 12th, the r^2 of inversion height to standard deviation of the 38.2 m wind speed (r^2=0.58) barely topped that of the 22.1 m measurement (r^2=0.50), indicating that, of the variables tested, the variability of the regional wind held the greatest link to inversion height on this night. To put these values into context, the r^2 of the standard deviation of the 38.2 m wind speed to inversion height was almost twice as high as the r^2 between the 38.2 m wind speed and the 22.1 m wind speed on the same night (r^2=0.33). So, the variation in the 38.2 m wind speed could explain much more of the variation in inversion height than it indicated about the wind speed at another height on that night (assuming a linear relationship). As both the wind speeds and the standard deviation appeared to have similar curves in the scatterplots, a comparison based on the coefficients of determination, while not ideal, may present a fair approximation of how closely each pair of variables is linked.

The negative correlation between wind speed and inversion supports the idea that inversion height is a compromise between the temperature gradient and wind shear. The density gradient that occurs under a strong positive temperature gradient works as a stabilizing force, while wind-shear induced turbulence acts against this, mixing the air. If the temperature gradient overpowers the mixing, it acts as a positive feedback, as more stability will allow for more stratification, thus increasing the stability. This principal is taken a step further by the model proposed by Schilperoort et al. (2022) for inversion formation. According to this model, sharp inversions are caused by an increased mixing due to turbulence at the forest floor and at the canopy. This increase in mixing leads to a sharper gradient in the temperature profile somewhere between these two points. If this new temperature gradient surpasses the point at which the density gradient generates a positive feedback loop, sharpening occurs. (For more complete information on this model's processes, see Section 4 and Figure 12 of Schilperoort et al. (2022).)

As expected, the nights without inversion showed no correlation between the (unscreened) inversion heights and other meteorological data. On average, the wind speed also exhibited a lower correlation to itself at other heights on these nights (for example, Figure A.16). The lack of correlation on nights without inversion, while saying little about those nights, lends significance to the correlations and coefficients of determination discovered on the inversion-rich evenings.

As is clear from the two examples studied, the specific characteristics of each inversion vary case-by-case. For these two cases, the inversion height and (variation in) wind speed displayed relatively strong correlations. While it seems likely that a lack of wind shear and resulting turbulence plays a key role in inversion formation, and the variability of wind a key role in inversion height, correlation does not beget causality. A resulting suggestion for further study would be to research whether either of these elements causes the other, or if they are together governed by some other factor. A lack of cloud cover and rainfall also seems to form a requirement for inversion formation, though that could simply be due to the low number of examples analysed. How the selection of the parameters used to screen for inversion plays into the calculated inversion parameters could also be further examined. For example, including only very strong inversions, or implementing a different window size, would likely affect the correlations, as well as the coefficients of determination. Perhaps even more interesting would be to test for coefficients of determination under different models, as the curved shape of the scatter plots indicates that a curved relationship may be more accurate than a linear one.

6

Conclusion

A multitude of exchanges of energy and mass make up the coupling between land and atmosphere. This coupling drives climate and weather, which play a decisive role in agriculture, health, ecology, and other sectors. Forest morphology, composition, and biology-related properties influence this coupling, and are challenging to measure and model. One key element of this coupling is heat transfer. Studying eddy characteristics and temperature profiles provides insight into how, when, and to which magnitude heat transfer occurs. The DTS holds the potential to provide information on eddies and the distribution of temperature in the atmosphere due to its high sensitivity and data resolution.

Data gathered from the DTS at Loobos during the first half of November displayed fluctuations in temperature, likely due to turbulent heat transfer eddies. Performing a difference calculation between the one second profiles and the rolling mean temperature helped remove the effects of tower features from the profile data. The magnitude and velocity of these eddies could not be determined based on the current methods. The one second temperature profiles indicated the atmospheric stability from a meter above the forest floor up to 1.5 times the canopy height. Viewing these profiles sequentially showed how the temperature gradients present developed over time.

The weather impacted the vertical distribution of temperature in the forest. The DTS captured these impacts, which often matched with theoretical expectations. Warming at the forest floor and canopy occurred during the day, specifically under direct sunlight. Nights displayed cooling at the forest floor and canopy, as well as the occasional formation of a sharp temperature inversion and decoupling. Different patterns of sensible heat transfer were occasionally also visible in the data, as evidenced by the “fingers” on days with less wind versus the grainy mixing of windy days. The DTS tended to overestimate the air temperature under direct sunlight, and may have underestimated the air temperature during and shortly after rain showers. When studying the DTS data, placing the measurements into meteorological context is essential.

Inversions formed on clear nights with very little wind. Inversion height throughout the canopy and understory strongly linked to wind speed and variation. The two cases of inversion studied differed in height, strength, and how well they correlated with the wind speed-related factors, implying that the properties of inversions with different characteristics may depend on airflow at different heights.

Combining various methods of viewing DTS data provides a thorough overview of temperature development throughout the day, and detailed information on the small temperature gradients often present in the forests. Adding extra meteorology data (such as radiation, wind speed, and rainfall) brings clarity and a method to verify the weather conditions indicated by the DTS. Gaining insight into temperature gradients and modes of heat transfer in the forest provides a way to assess and improve weather and climate models. Next to passive applications such as predicting the weather, these models can be used to anticipate the effects of actions such as reforesting landscapes or implementing urban greening.

6.1. Recommendations for further research

The following list indicates potential next steps to gain further insight into the topics studied in this thesis.

- Creating a 2D or 3D DTS set-up in a forested region may yield more insight into turbulent eddies in the forest.
- Performing this research over a more extended period could test if the patterns uncovered in this project persist under similar weather conditions, as well as discover what role seasonality and the greening of the understory might play.
- Testing additional nights and other locations with inversion to search for correlations between inversion height, strength, and meteorological properties could help further understanding of which aspects of the weather influence low-laying nighttime inversions.
- Exploring correlations between turbulent kinetic energy, wind shear, and inversion height may provide further understanding into which elements contribute to inversion strength and height.
- Performing a study similar to this one, but with a fiber measuring the wet bulb temperature, would allow for the addition of the relative humidity. In this manner, insight could be gained into the transport of moisture and subsequent latent heat flux.

7

References

Abubaker, A., Kosti, I., & Kosti, O. (2018, July). Numerical modelling of velocity profile parameters of the atmospheric boundary layer simulated in wind tunnels. *IOP Conference Series: Materials Science and Engineering*, *393*(1), 012025. (Publisher: IOP Publishing) doi: 10.1088/1757-899X/393/1/012025

Butterworth, B. J., Desai, A. R., Metzger, S., Townsend, P. A., Schwartz, M. D., Petty, G. W., ... Zheng, T. (2021, February). Connecting LandAtmosphere Interactions to Surface Heterogeneity in CHEESEHEAD19. *Bulletin of the American Meteorological Society*, *102*(2), E421–E445. (Publisher: American Meteorological Society Section: Bulletin of the American Meteorological Society) doi: 10.1175/BAMS-D-19-0346.1

Cava, D., Giostra, U., Siqueira, M., & Katul, G. (2004, July). Organised Motion and Radiative Perturbations in the Nocturnal Canopy Sublayer above an Even-Aged Pine Forest. *Boundary-Layer Meteorology*, *112*(1), 129–157. doi: 10.1023/B:BOUN.0000020160.28184.a0

Curto, L., & Gassmann, M. I. (2022, August). Wavelet Analysis of Coherent Structures Above Maize and Soybean Crops. *Boundary-Layer Meteorology*, *184*(2), 231–249. doi: 10.1007/s10546-022-00705-w

da Rocha, H. R., Goulden, M. L., Miller, S. D., Menton, M. C., Pinto, L. D. V. O., de Freitas, H. C., & e Silva Figueira, A. M. (2004). Seasonality of Water and Heat Fluxes Over a Tropical Forest in Eastern Amazonia. *Ecological Applications*, *14*(4), 22–32.

des Tombe, B., Schilperoort, B., & Bakker, M. (2020, January). Estimation of Temperature and Associated Uncertainty from Fiber-Optic Raman-Spectrum Distributed Temperature Sensing. *Sensors*, *20*(8), 2235. (Number: 8 Publisher: Multidisciplinary Digital Publishing Institute) doi: 10.3390/s20082235

Euser, T., Luxemburg, W. M. J., Everson, C. S., Mengistu, M. G., Clulow, A. D., & Bastiaanssen, W. G. M. (2014). A new method to measure Bowen ratios using high-resolution vertical dry and wet bulb temperature profiles. *Hydrology and Earth System Sciences*, *18*(6), 2021–2032. (Number: 6) doi: 10.5194/hess-18-2021-2014

FAO. (2020). *Global Forest Resources Assessment 2020 - Key Findings*. Rome, Italy: Author. Retrieved 2023-02-05, from https://doi.org/10.4060/ca8753en

Foken, T. (Ed.). (2021). *Springer Handbook of Atmospheric Measurements*. Cham: Springer International Publishing. doi: 10.1007/978-3-030-52171-4

Foken, T., Beyrich, F., & Wulfmeyer, V. (2021). Introduction to Atmospheric Measurements. In T. Foken (Ed.), *Springer Handbook of Atmospheric Measurements* (pp. 3–31). Cham: Springer International Publishing. doi: 10.1007/978-3-030-52171-4_1

Google. (n.d.). *Google maps.* Author. Retrieved 2023-01-23, from https://www.google.com/maps/@52.1718661,5.7353567,5706m/data=!3m1!1e3

Green, J. K., Konings, A. G., Alemohammad, S. H., Berry, J., Entekhabi, D., Kolassa, J., ... Gentine, P. (2017, May). Regionally strong feedbacks between the atmosphere and terrestrial biosphere. *Nature geoscience*, *Volume 10*(Iss 6), 410–414. doi: 10.1038/ngeo2957

Hilland, R. V. J., Bernhofer, C., Bohmann, M., Christen, A., Katurji, M., Maggs-Kölling, G., ... Vogt, R. (2022, March). The Namib Turbulence Experiment: Investigating SurfaceAtmosphere Heat Transfer in Three Dimensions. *Bulletin of the American Meteorological Society*, *103*(3), E741–E760. (Publisher: American Meteorological Society Section: Bulletin of the American Meteorological Society) doi: 10.1175/BAMS-D-20-0269.1

Izett, J. G., Schilperoort, B., Coenders-Gerrits, M., Baas, P., Bosveld, F. C., & van de Wiel, B. J. H. (2019, November). Missed Fog? *Boundary-Layer Meteorology*, *173*(2), 289–309. doi: 10.1007/s10546-019-00462-3

Katul, G., Hsieh, C.-I., Oren, R., Ellsworth, D., & Phillips, N. (1996, August). Latent and sensible heat flux predictions from a uniform pine forest using surface renewal and flux variance methods. *Boundary-Layer Meteorology*, *80*(3), 249–282. doi: 10.1007/BF00119545

Kleissl, J., & Garai, A. (2011, December). Air and Surface Temperature Coupling in the Convective Atmospheric Boundary Layer. *Journal of the Atmospheric Sciences*, *68*, 2945–54. doi: 10.1175/JAS-D-11-057.1

Klimaatviewer. (n.d.). Retrieved 2023-02-05, from https://www.knmi.nl/klimaat-viewer/kaarten/temperatuur/gemiddelde-temperatuur/jaar/Periode_1991-2020

KNMI - Uurgegevens van het weer in Nederland. (n.d.). Retrieved 2023-04-10, from https://www.knmi.nl/nederland-nu/klimatologie/uurgegevens

Lienhard IV, J. H., & Lienhard V, J. H. (2020). *A Heat Transfer Textbook, 5th edition* (5th ed.). Cambridge Massachussets: Phlogiston Press. Retrieved 2023-01-29, from https://ahtt.mit.edu/

Meier, F., & Scherer, D. (2012, December). Spatial and temporal variability of urban tree canopy temperature during summer 2010 in Berlin, Germany. *Theoretical and Applied Climatology*, *110*(3), 373–384. doi: 10.1007/s00704-012-0631-0

Moene, A. F., & Dam, J. C. v. (2014). *Transport in the Atmosphere-Vegetation-Soil Continuum.* Cambridge: Cambridge University Press.

Oliphant, A. J., Grimmond, C. S. B., Zutter, H. N., Schmid, H. P., Su, H. B., Scott, S. L., ... Ehman, J. (2004, November). Heat storage and energy balance fluxes for a temperate deciduous forest. *Agricultural and Forest Meteorology*, *126*(3), 185–201. doi: 10.1016/j.agrformet.2004.07.003

Peltola, O., Aurela, M., Launiainen, S., & Katul, G. (2022). Probing eddy size and its effective mixing length in stably stratified roughness sublayer flows. *Quarterly Journal of the Royal Meteorological Society*, *148*(749), 3756–3773. (_eprint: https://onlinelibrary.wiley.com/doi/pdf/10.1002/qj.4386) doi: 10.1002/qj.4386

Peltola, O., Lapo, K., Martinkauppi, I., O'Connor, E., Thomas, C. K., & Vesala, T. (2021, March). Suitability of fibre-optic distributed temperature sensing for revealing mixing processes and higher-order moments at the forestair interface. *Atmospheric Measurement Techniques*, *14*(3), 2409–2427. (Publisher: Copernicus GmbH) doi: 10.5194/amt-14-2409-2021

Puma, M. J., Koster, R. D., & Cook, B. I. (2013). Phenological versus meteorological controls on land-atmosphere water and carbon fluxes. *Journal of Geophysical Research: Biogeosciences*, *118*(1), 14–29. (_eprint: https://onlinelibrary.wiley.com/doi/pdf/10.1029/2012JG002088) doi: 10.1029/2012JG002088

Schilperoort, B., Coenders-Gerrits, M., Jiménez Rodríguez, C., van der Tol, C., van de Wiel, B., & Savenije, H. (2020, December). Decoupling of a Douglas fir canopy: a look into the subcanopy with continuous vertical temperature profiles. *Biogeosciences*, *17*(24), 6423–6439. (Publisher: Copernicus GmbH) doi: 10.5194/bg-17-6423-2020

Schilperoort, B., Coenders-Gerrits, M., Luxemburg, W., Jiménez Rodríguez, C., Cisneros Vaca, C., & Savenije, H. (2018, January). Technical note: Using distributed temperature sensing for Bowen ratio evaporation measurements. *Hydrology and Earth System Sciences*, *22*(1), 819–830. (Publisher: Copernicus GmbH) doi: 10.5194/hess-22-819-2018

Schilperoort, B., Coenders-Gerrits, M., Rodríguez, C. J., Hooft, A. v., Wiel, B. v. d., & Savenije, H. (2022). Detecting nighttime inversions in the interior of a Douglas fir canopy. *Agricultural and Forest Meteorology*, *321*, 108960. doi: https://doi.org/10.1016/j.agrformet.2022.108960

Site Loobos. (n.d.). Retrieved 2023-04-10, from http://www.climatexchange.nl/sites/loobos/index.htm

Thomas, C. K., Kennedy, A. M., Selker, J. S., Moretti, A., Schroth, M. H., Smoot, A. R., ... Zeeman, M. J. (2012, February). High-Resolution Fibre-Optic Temperature Sensing: A New Tool to Study the Two-Dimensional Structure of Atmospheric Surface-Layer Flow. *Boundary-Layer Meteorology*, *142*(2), 177–192. doi: 10.1007/s10546-011-9672-7

Thomas, C. K., & Selker, J. (2021, November). Optical Fiber-Based Distributed Sensing Methods. In (pp. 611–633). Cham, Switzerland: Springer.

Torrence, C., & Compo, G. P. (1998). A Practical Guide to Wavelet Analysis. *Bulletin of the American Meteorological Society*, *79*(1), 61–78. (Publisher: American Meteorological Society)

Ukil, A., Braendle, H., & Krippner, P. (2012, May). Distributed Temperature Sensing: Review of Technology and Applications. *IEEE Sensors Journal*, *12*(5), 885–892. (Conference Name: IEEE Sensors Journal) doi: 10.1109/JSEN.2011.2162060

van Ramshorst, J. G. V., Coenders-Gerrits, M., Schilperoort, B., van de Wiel, B. J. H., Izett, J. G., Selker, J. S., ... van de Giesen, N. C. (2020, October). Revisiting wind speed measurements using actively heated fiber optics: a wind tunnel study. *Atmospheric Measurement Techniques*, *13*(10), 5423–5439. (Publisher: Copernicus GmbH) doi: 10.5194/amt-13-5423-2020

Williams, I. N., & Torn, M. S. (2015). Vegetation controls on surface heat flux partitioning, and land-atmosphere coupling. *Geophysical Research Letters*, *42*(21), 9416–9424. (_eprint: https://onlinelibrary.wiley.com/doi/pdf/10.1002/2015GL066305) doi: 10.1002/2015GL066305

Zhang, C., & Jin, Z. (2019, January). RDTS-Based Two-Dimensional Temperature Monitoring with High Positioning Accuracy Using Grid Distribution. *Sensors*, *19*(22), 4993. (Number: 22 Publisher: Multidisciplinary Digital Publishing Institute) doi: 10.3390/s19224993

A

Appendix

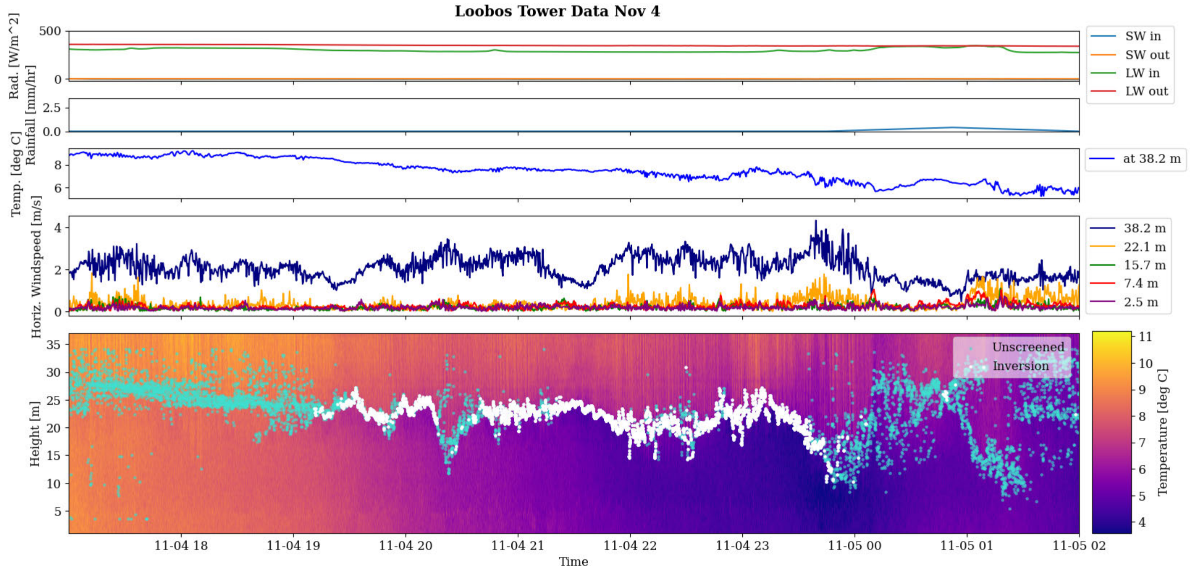

Figure A.1: Points with the largest temperature difference for each time step show up in light blue, with the selected points based on a minimum temperature difference in white.

A.1. All Days

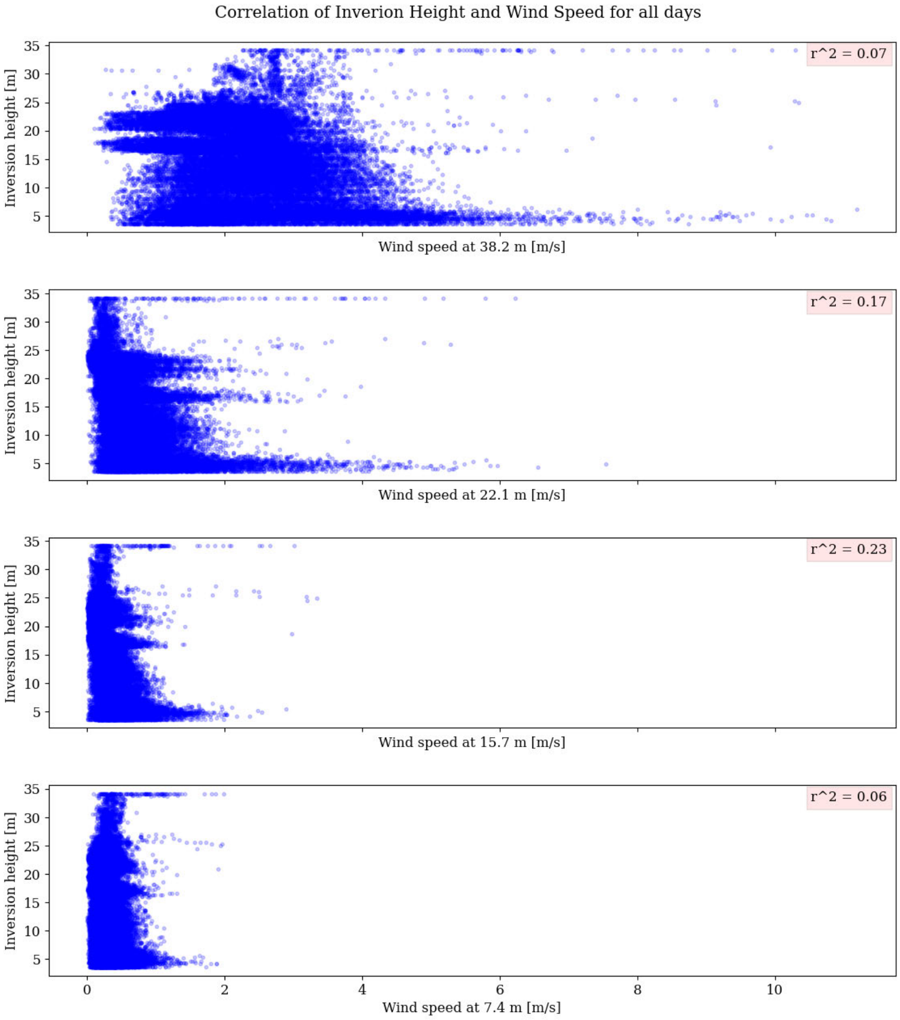

Figure A.2: Wind speed versus inversion height for October 30th through November 17th.

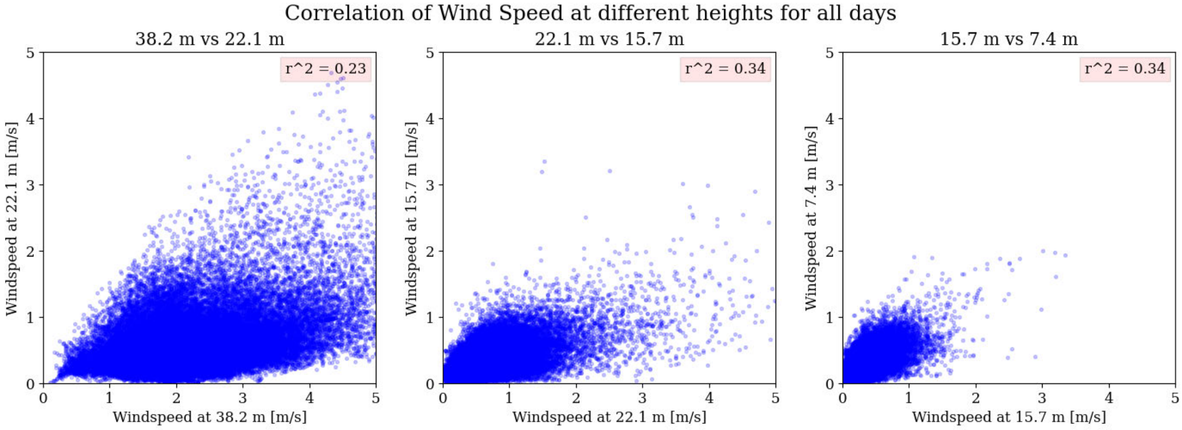

Figure A.3: Wind speed versus wind speed at one height step removed for October 30th through November 17th.

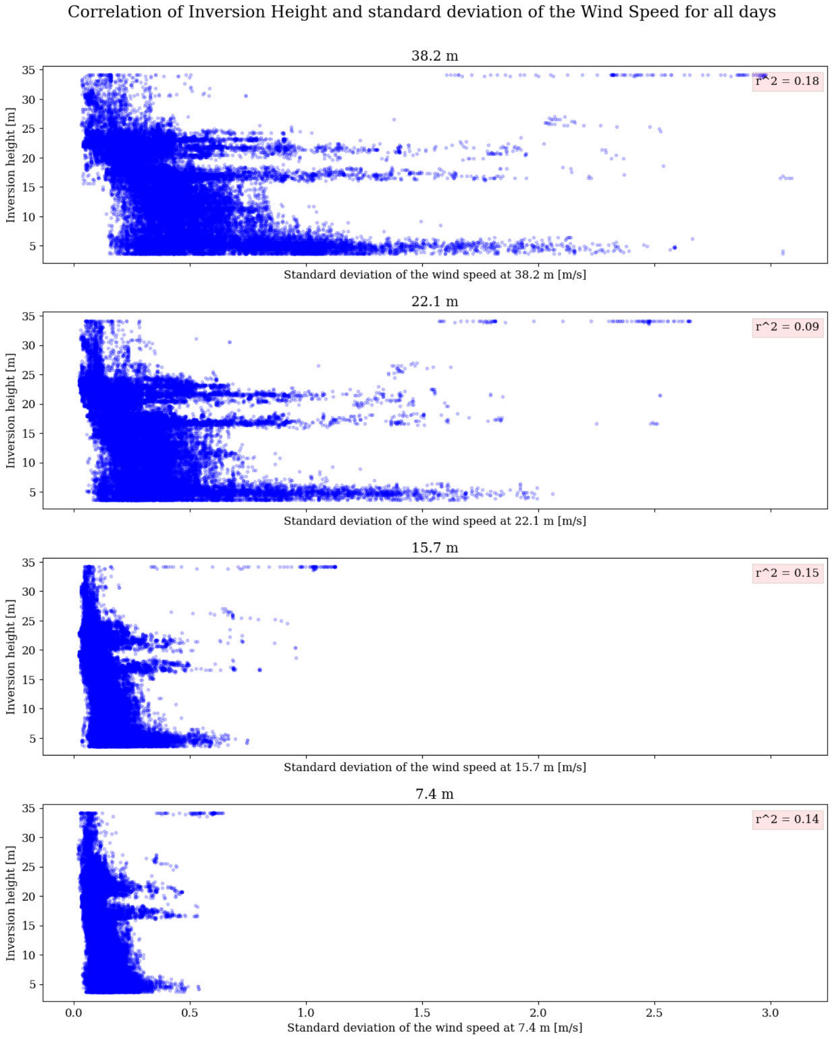

Figure A.4: Standard deviation versus inversion height for October 30th through November 17th.

A.2. November 4th

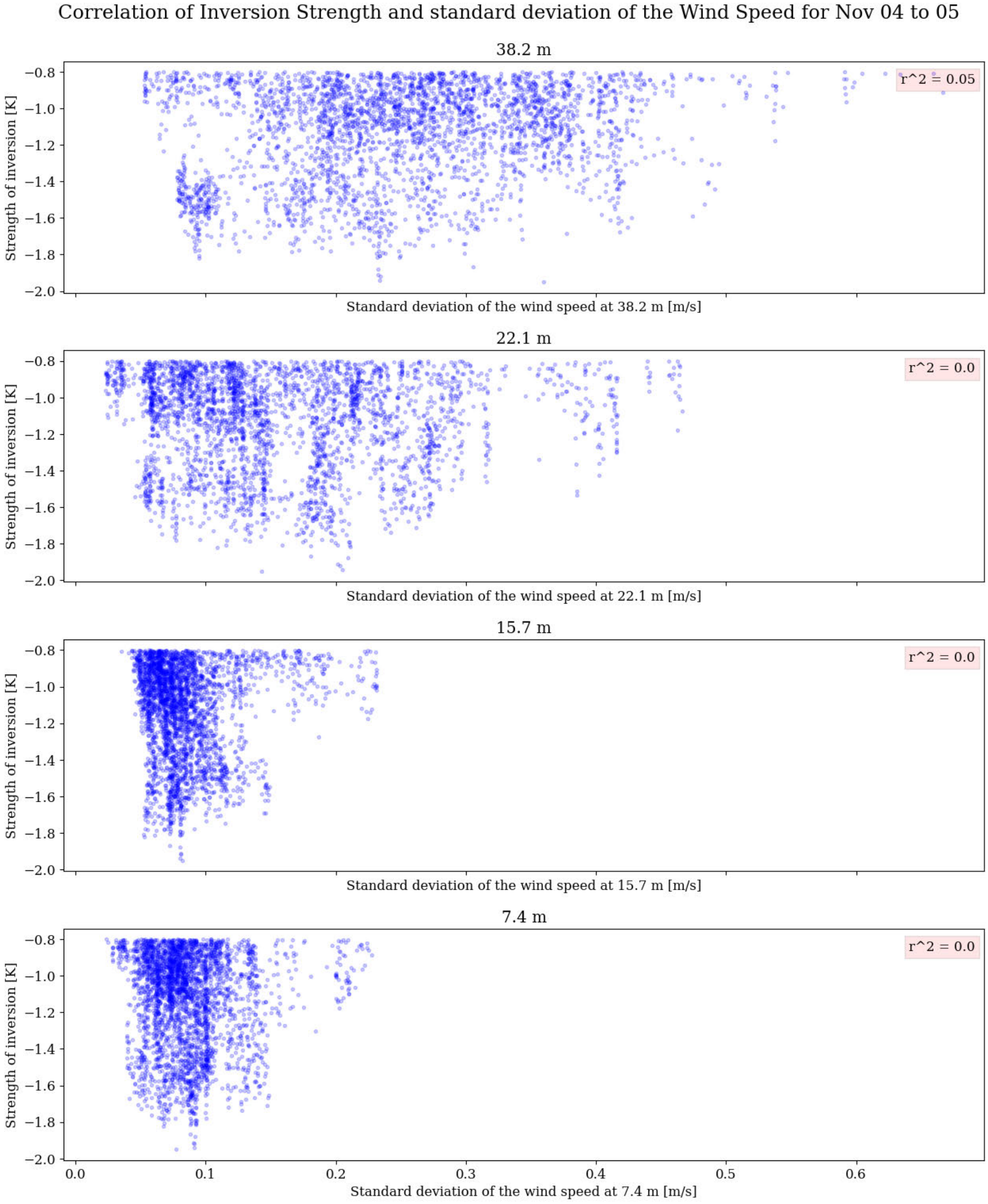

Figure A.5: Standard deviation of the wind speed and inversion strength on November 4th to 5th.

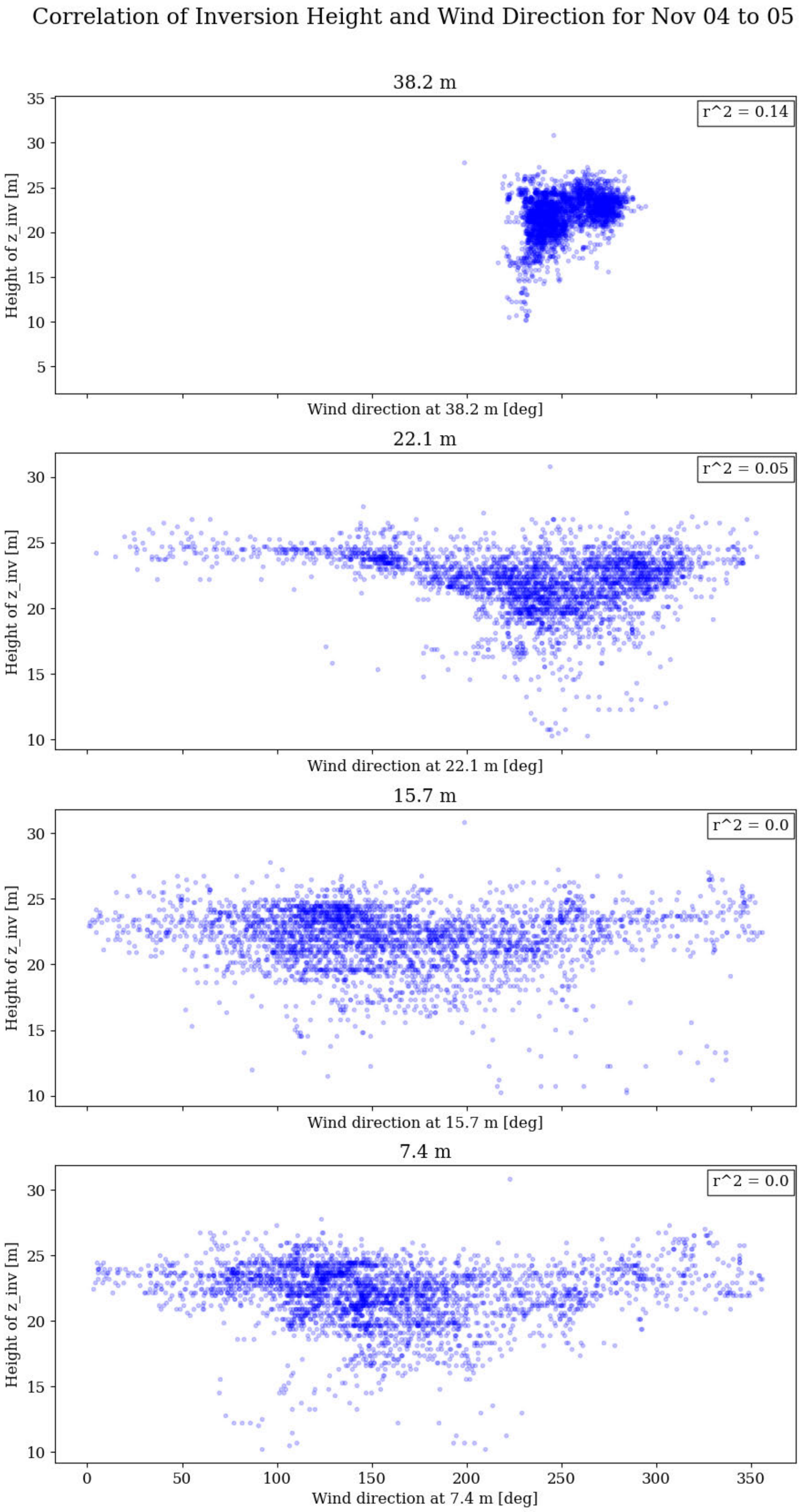

Figure A.6: Wind direction and inversion height on November 4th to 5th.

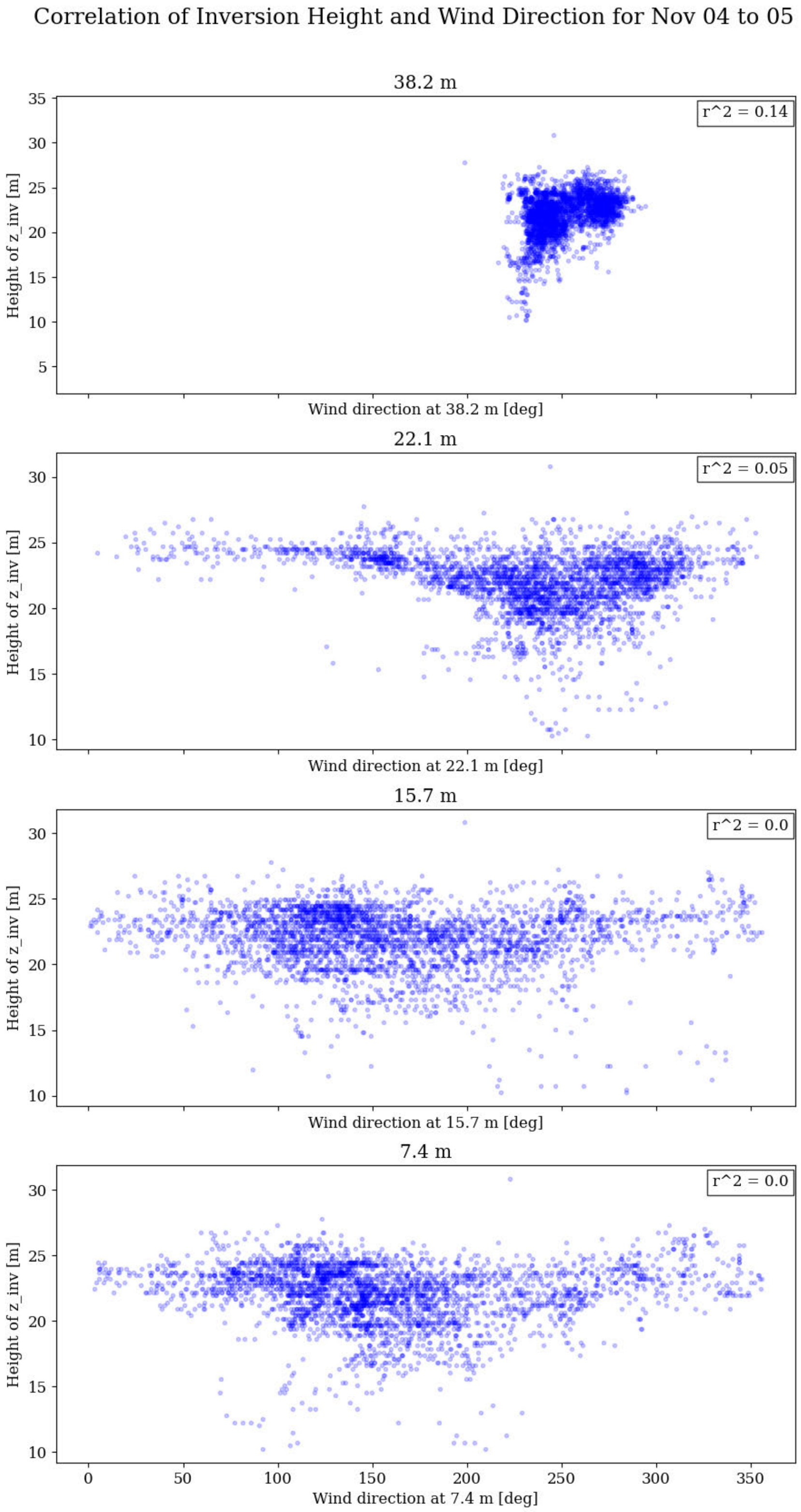

Figure A.7: Wind direction versus inversion height on November 4th to 5th.

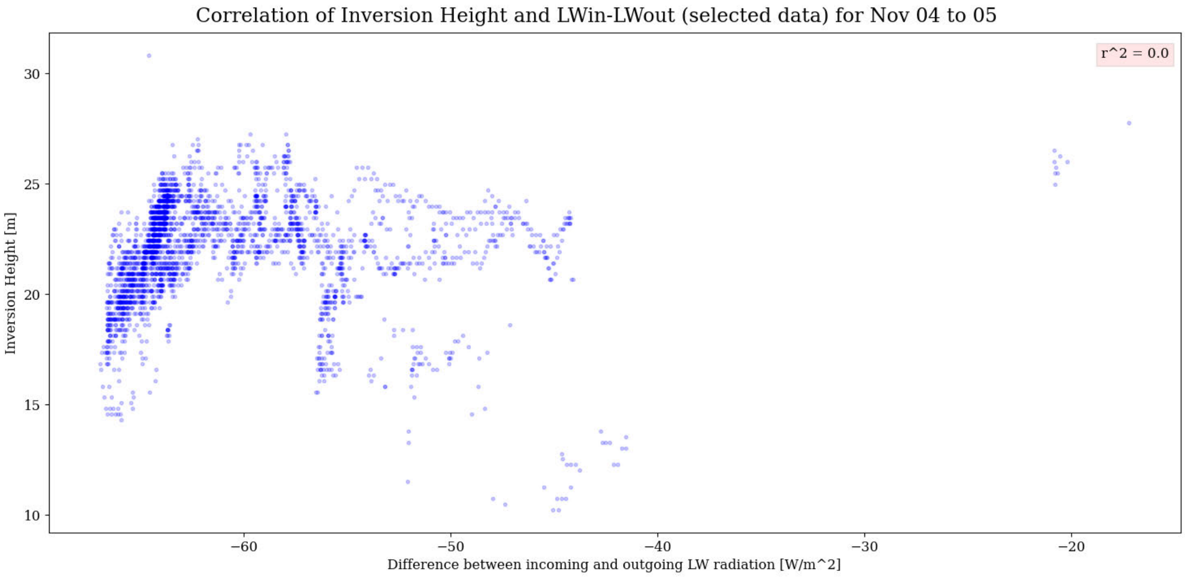

Figure A.8: Difference in longwave radiation versus inversion height on November 4th to 5th.

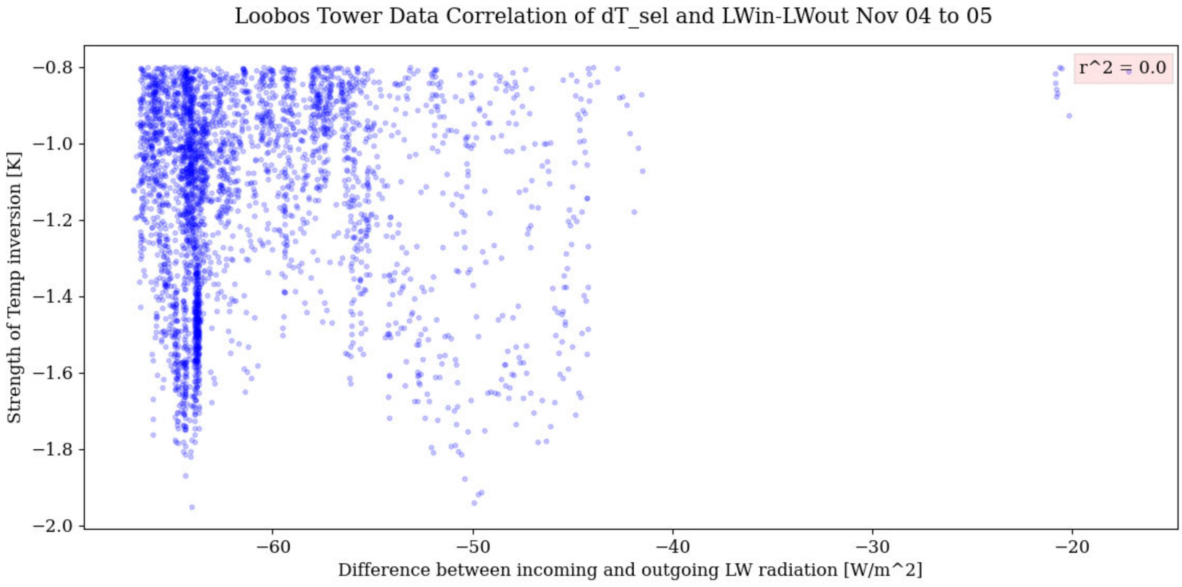

Figure A.9: Difference in longwave radiation versus inversion strength on November 4th to 5th.

A.3. November 12th

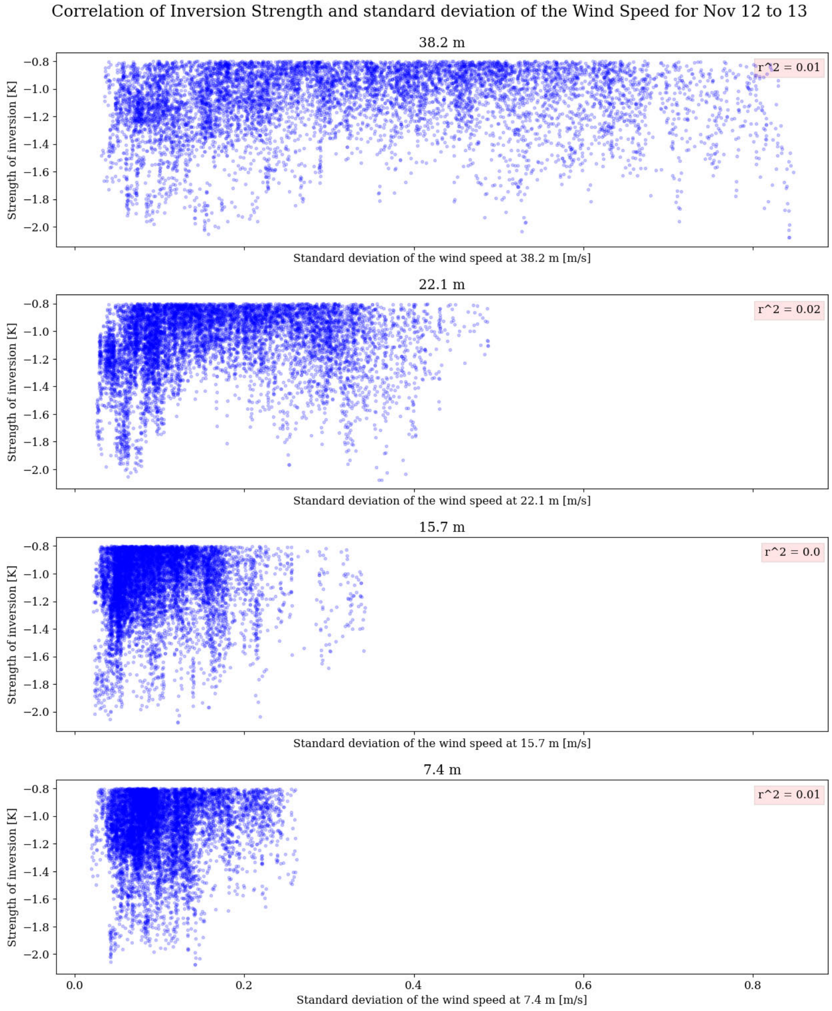

Figure A.10: Standard deviation of the wind speed correlated to the inversion strength on November 12th to 13th.

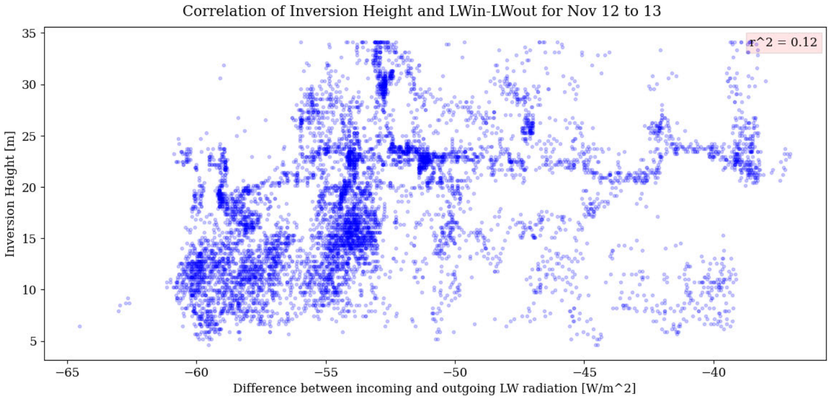

Figure A.11: Difference between incoming and outgoing longwave radiation and inversion height on November 12th to 13th.

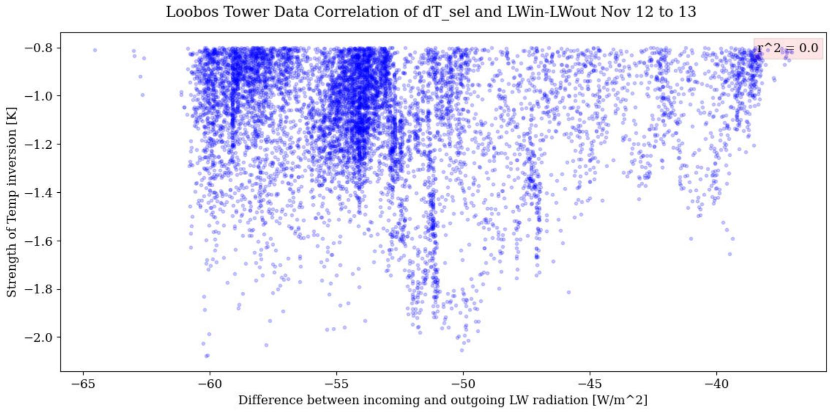

Figure A.12: Difference between incoming and outgoing longwave radiation and inversion strength on November 12th to 13th.

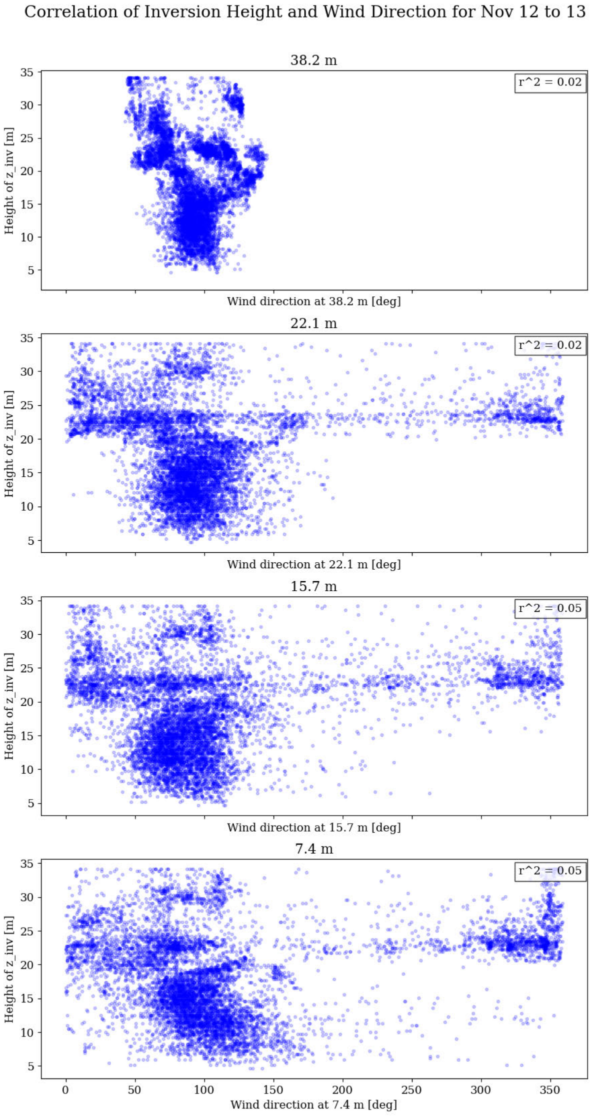

Figure A.13: Wind direction and inversion height on November 12th to 13th.

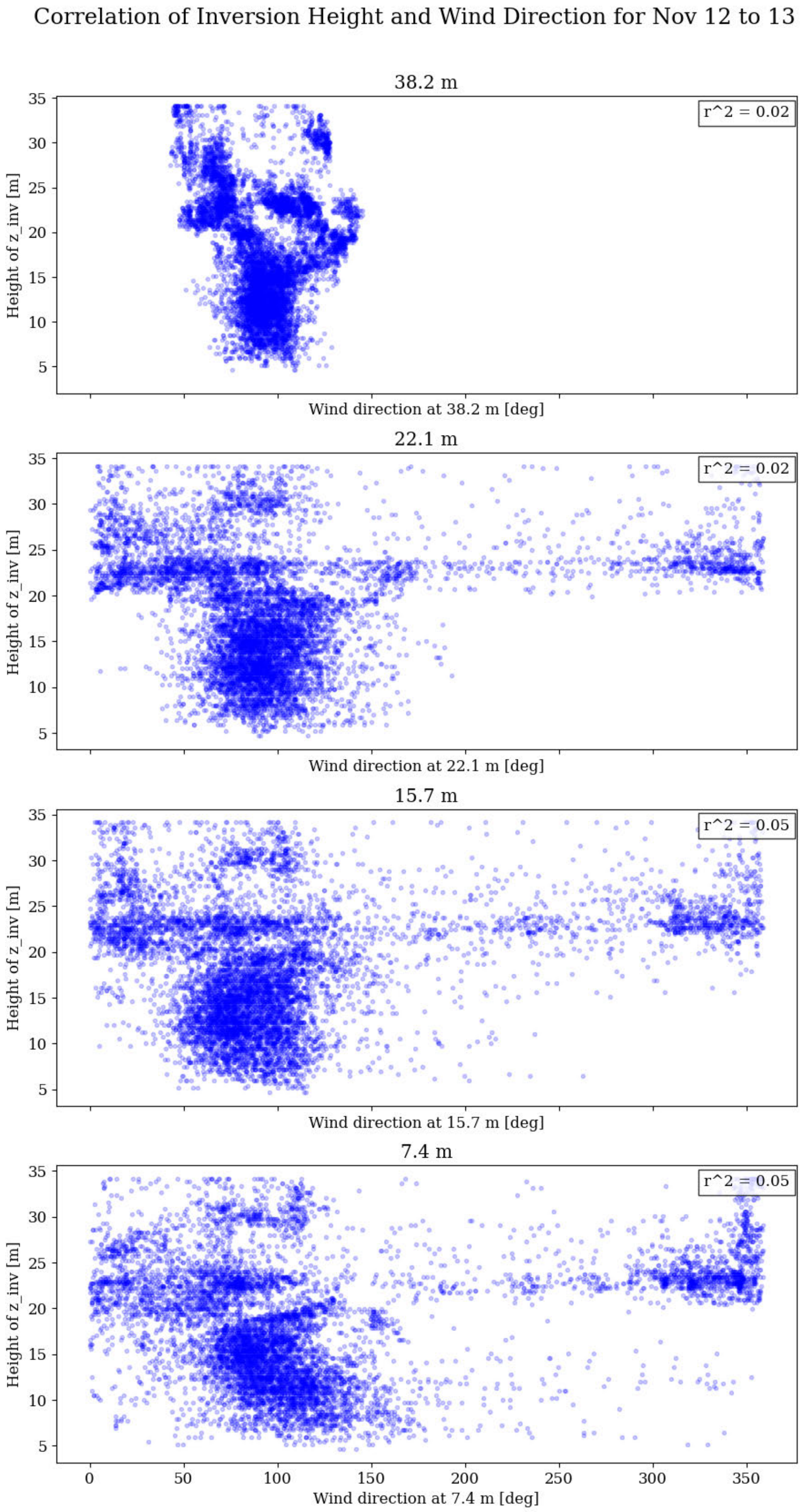

Figure A.14: Wind direction and inversion strength on November 12th to 13th.

A.4. November 6th

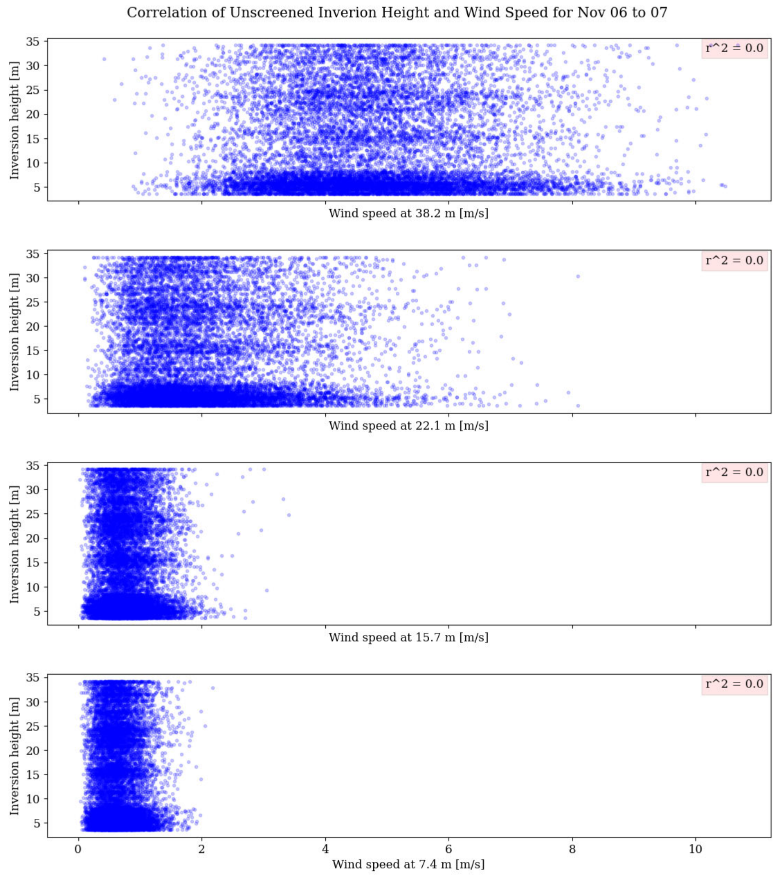

Figure A.15: Wind speed versus calculated inversion height for all data points on November 6th to 7th (not screened based on a minimum temperature).

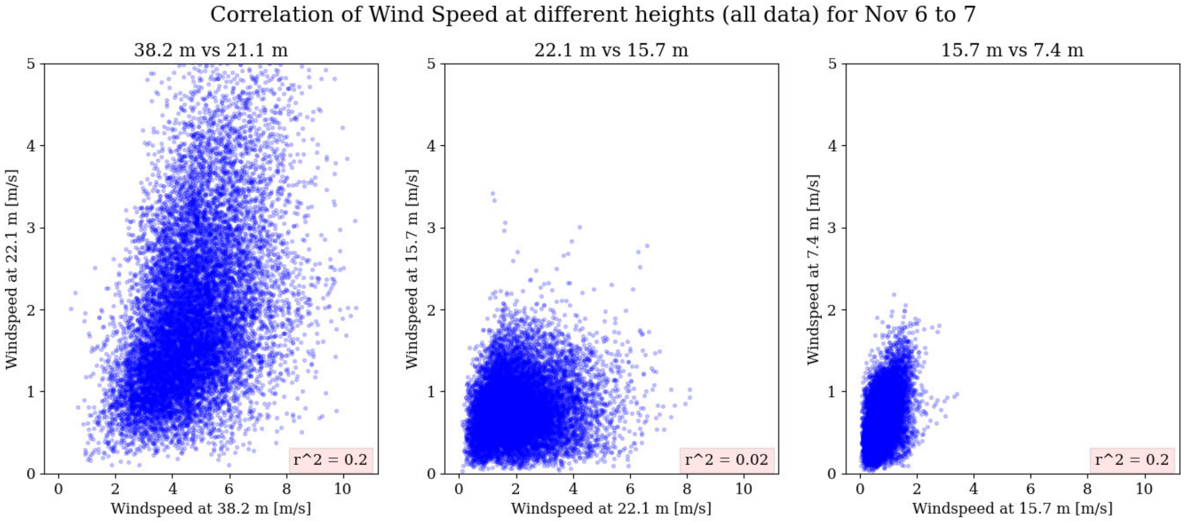

Figure A.16: Wind speed versus wind speed for all points on November 6th to 7th (not screened based on a minimum temperature).

Table A.1: Coefficients of determination for unscreened data between various meteorological variables for November 6th, a night on which no inversion was detected. The "Inversion Height" is the result of the inversion height calculated without temperature screening applied. The unscreened inversion r^2's for the inversion nights are shown in the two rightmost columns.

	r^2 for November 6th [-]					
Wind speed meas. height [m]	Inversion heights	22.1 m wind speed	15.7 m wind speed	7.4 m wind speed	Nov. 4 Inv. H.	Nov 12 Inv. H.
38.2	0.00	0.20	0.06	0.04	.12	.21
22.1	0.00	1	0.02	0.03	0.01	0.28
15.7	0.00	0.02	1	0.20	0.01	0.20
7.4	0.00	0.03	0.20	1	0.00	0.04